Research Article

Mohamed I. Nouh, Emad A-B. Abdel-Salam, Abaker A. Hassaballa*, and Mohamed S. Jazmati

Analysis of the fractional relativistic isothermal gas sphere with application to neutron stars

https://doi.org/10.1515/phys-2025-0170
received April 10, 2025; accepted May 16, 2025

Abstract: The isothermal gas sphere model may be beneficial for understanding certain features of astrophysical objects like stars, but it has severe limits when used for compact stars. This study expands the Tolman–Oppenheimer–Volkoff (TOV) equation of the fractional relativistic gas sphere to contain fractional derivatives, resulting in a more general fractional TOV equation (FTOVI). The analytical solution of the FTOVI equation is tackled using an accelerated series expansion. We computed models for various relativistic (σ) and fractional (α) parameters. Models with $\alpha = 1$ are retained to the relativistic integer models calculated by the integer version of the TOV equation. We examine the effects of the relativistic and fractional parameters on the Emden function, mass function, and the first derivative of the Emden function and the impact of these quantities on the pressure, density, and mass-radius relation. Investigating the central density-mass relation as an analog to neutron stars indicates that a maximum mass of the sphere exists, which further increases central density, resulting in instability and collapse. The observed mass and radius of three neutron stars and those predicted from the FTOVI models agreed well. The results of high-density fractional models demonstrate that fractional derivatives might drastically modify the expected mass and radius of neutron stars compared to integer models, indicating a possible need to reinterpret observational data of neutron stars *via* the lens of fractional calculus.

Keywords: isothermal gas sphere, neutron stars, stellar structure, series expansion, fractional calculus

*** Corresponding author: Abaker A. Hassaballa,** Center for Scientific Research and Entrepreneurship, Northern Border University, Arar, 73213, Saudi Arabia; Department of Mathematics, College of Science, Northern Border University, Arar, 73213, Saudi Arabia, e-mail: abaker.abdalla@nbu.edu.sa
Mohamed I. Nouh: Astronomy Department, National Research Institute of Astronomy and Geophysics, Helwan, Cairo, 11421, Egypt
Emad A-B. Abdel-Salam: Department of Mathematics, Faculty of Science, New Valley University, El-Kharja, 72511, Egypt
Mohamed S. Jazmati: Department of Mathematics, College of Science, Qassim University, P.O. Box 6644, Buraydah, 51452, Saudi Arabia

1 Introduction

Isothermal gas spheres play a vital role in understanding the dynamics and structure of self-gravitating systems, such as stars, galaxies, and clusters. However, the classical isothermal sphere model has limitations because it overlooks relativistic effects in strong gravitational fields, particularly around massive compact objects like black holes and neutron stars. The relativistic isothermal gas sphere (RISG) model overcomes these shortcomings by incorporating the effects of general relativity into the classical framework.

In the framework of general relativity, Chandrasekhar [1] developed the RISG, which integrates the effects of relativistic gravity and pressure, resulting in a more realistic model for high-energy astrophysical systems. This relativistic approach significantly alters pressure and density distributions, a topic `further explored in subsequent studies [2,3]. The importance of these relativistic modifications becomes particularly pronounced when analyzing compact stars, such as neutron stars, and certain phases of stellar collapse, where gravitational fields and internal gas pressures approach relativistic levels [4,5]. Chau *et al.* [6] built upon the research of Edwards and Merilan [7,8] to investigate the static structure of general relativistic, partially degenerate isothermal configurations with arbitrary temperatures. Sharma [9] examined the analytic structure of high-density isothermal gas spheres within the context of general relativity. Chavanis' studies [10–12] revealed that the RISG, similar to neutron cores, exhibits behaviors akin to Newtonian isothermal spheres.

Over the past three decades, fractional differential equations have gained traction across various scientific and technical fields, including mathematics, chemistry, optics, plasma, and fluid dynamics. There has been growing interest in applying fractional calculus within astronomy [13], for example, Jamil *et al.* [14] introduced a dark energy model featuring relevant cosmological parameters by employing a power-law weight function within the framework of fractional action cosmology. El-Nabulsi [15] presented a novel theory of substantial gravity, highlighting the distinction between zero and fractional graviton

masses in extremely low cosmic fluid density. Addressing dynamical functional equations involving fractional derivatives or based on Einstein-Hilbert behavior [16,17] consistently yielded effective solutions. Furthermore, El-Nabulsi [18] derived nonlocal fractional Einstein's field equations by generalizing the standard Einstein field equations through fractional derivatives. He also explored the family of Emden-Fowler differential equations, presenting a generalized derivative operator [19]. In addition, El-Nabulsi [20] examined the rapid expansion of a non-singular universe, both with and without scalar fields, utilizing an Ornstein-Uhlenbeck-like fractional differential equation, a generalized fractional scale factor, and a time-dependent Hubble parameter.

Mirza [21] investigated the fractional isothermal gas sphere by solving it through iteration using a two-term series expansion, continuing until the Emden function at the sphere's center reached appropriate values. Nouh [22] discussed the potential applications of fractional models in stellar computations, particularly in solving the system of fractional differential equations that model the helium-burning phase in stars. Yousif *et al.* [23] developed general analytical formulations for the fractional isothermal gas sphere within Newtonian hydrostatic equilibrium. El-Nabulsi [24] explored the fractional Lane-Emden equations of white dwarf stars, while Bayin and Krisch [25] focused on the incompressible gas sphere. Nouh and Abdel-Salam [26,27] examined the fractional isothermal gas sphere and the polytropic gas sphere using modified Riemann-Liouville fractional derivatives and Abdel-Salam and Nouh [28] analyzed conformable polytropic gas spheres. A conformable Adomian decomposition technique was applied by Abdel-Salam *et al.* [29] to derive a divergent series solution for Lane–Emden type equations. Aboueisha *et al.* [30] investigated the fractional relativistic polytropic gas sphere and assessed the influence of the fractional parameter on the mass-radius relationship of white dwarfs.

In this work, we incorporate fractional calculus into the RISG model to explore the effects of long-range interactions and nonlocal gravitational behavior. By introducing fractional derivatives into the equations governing the system's equilibrium, we aim to investigate how the fractional order impacts the structural characteristics of the gas sphere, including density profiles, gravitational potentials, and stability criteria. Under the physical conditions of the neutron stars, we compare the mass-radius relation of the fractional RISG (FRISG) with the observed masses and radii of three neutron stars.

This study is organized as follows: Section 2 introduces the concept of fractional derivatives. Section 3 proposes the FRISG models. Section 4 outlines the series expansion method employed to solve the modified equations and discusses the results obtained. Section 5 analyzes the numerical results. Section 6 gives an application to the neutron star structure. The conclusion of the study is presented in Section 7.

2 Conformable fractional calculus (CFD)

CFD is an extension of traditional calculus that allows for the differentiation and integration of functions with fractional orders while preserving certain classical properties. Unlike classical fractional calculus, which often relies on complex definitions and can introduce complications in analysis, conformable fractional derivatives are defined in a way that aligns more closely with classical derivatives. This makes them more intuitive and easier to apply in various contexts. Applications of CFD span multiple fields, including physics, engineering, and finance, where it is used to model phenomena with memory effects or long-range interactions. For instance, in physics, it can describe nonlinear diffusion processes, while in engineering, it aids in analyzing systems exhibiting viscoelastic behavior.

Khalil *et al.* [31] introduced CFD by applying limits in the form

$$D^{\alpha}v(t) = \lim_{\varepsilon \to 0} \frac{v(t + \varepsilon t^{1-\alpha}) - v(t)}{\varepsilon} \quad \forall\, t > 0, \quad \alpha \in [0, 1], \quad v^{(\alpha)}(0) = \lim_{t \to 0^{+}} v^{(\alpha)}(t). \tag{1}$$

Here $v^{(\alpha)}(0)$ is not defined. When $\alpha = 1$, this fractional derivative reduces to the ordinary derivative. The CFD has the following properties:

$$D^{\alpha}\, t^{p} = pt^{p-\alpha}, \quad p \in \mathbb{R}, \quad D^{\alpha}c = 0, \quad \forall v(t) = c, \tag{2}$$

$$D^{\alpha}(av + bg) = aD^{\alpha}v + bD^{\alpha}g, \quad \forall a, b \in \mathbb{R}, \tag{3}$$

$$D^{\alpha}(vg) = vD^{\alpha}g + gD^{\alpha}v, \tag{4}$$

$$D^{\alpha}v(g) = \frac{\mathrm{d}v}{\mathrm{d}g} D^{\alpha}g, \quad D^{\alpha}v(t) = t^{1-\alpha}\frac{\mathrm{d}v}{\mathrm{d}t}, \tag{5}$$

where v, g are two α-differentiable functions and c is an arbitrary constant. Eqs (4) and (5) are proved in the study by Khalil *et al.* [31]. The CFD of some functions are as follows:

$$\begin{aligned} &D^{\alpha}e^{ct} = ct^{1-\alpha}e^{ct}, \quad D^{\alpha}\ \sin(ct) = ct^{1-\alpha}\ \cos(ct), \\ &D^{\alpha}\ \cos(ct) = -ct^{1-\alpha}\ \sin(ct), \\ &D^{\alpha}e^{ct^{\alpha}} = cae^{ct^{\alpha}}, \quad D^{\alpha}\ \sin(ct^{\alpha}) = c\alpha\ \cos(ct^{\alpha}), \\ &D^{\alpha}\ \cos(ct^{\alpha}) = -c\alpha\ \sin(ct^{\alpha}). \end{aligned} \tag{6}$$

3 Conformable FRISG

In the context of the fractional derivative, line elements describing the interior space-time of a static spherically symmetric star in standard coordinates $(t, r, \vartheta, \varphi)$ can be expressed in the following form [30]:

$$d^{\alpha}s^2 = e^{2\nu(r^{\alpha})}(cd^{\alpha}t)^2 - e^{2\lambda(r^{\alpha})}d^{\alpha}r^2 - r^{2\alpha}d^{\alpha}\vartheta^2 - r^{2\alpha}\sin^2(\vartheta^{\alpha})d^{\alpha}\varphi^2, \tag{7}$$

where ν and λ are functions of r^{α} that characterize the gravitational field and the geometry of the star's interior, which is governed by the fractional Einstein's field equation. The fractional metric tensor captures the essential features of a spherically symmetric object, allowing us to explore the effects of fractional calculus on the structure and dynamics of the star. By incorporating fractional derivatives into the equations governing this space-time, we can investigate modifications to the physical properties such as pressure, density, and stability, providing deeper insights into the behavior of compact stellar objects.

Thus, the relation between the fractional metric tensor ${}^{\alpha}g_{\mu\nu}$ and the fractional line element is

$$d^{\alpha}s^2 = {}^{\alpha}g_{\mu\nu}d^{\alpha}x^{\mu}d^{\alpha}x^{\nu}. \tag{8}$$

By comparing Eqs. (7) and (8), ${}^{\alpha}g_{\mu\nu}$ is to be

$${}^{\alpha}g_{\mu\nu} = \begin{pmatrix} e^{2\nu(r^{\alpha})} & 0 & 0 & 0 \\ 0 & -e^{2\lambda(r^{\alpha})} & 0 & 0 \\ 0 & 0 & -r^{2\alpha} & 0 \\ 0 & 0 & 0 & -r^{2\alpha}\sin^2(\vartheta^{\alpha}) \end{pmatrix}. \tag{9}$$

Therefore, the nonzero elements of the fractional metric are

$$\begin{aligned} {}^{\alpha}g_{tt} &= {}^{\alpha}g_{11} = e^{2\nu(r^{\alpha})}, \quad {}^{\alpha}g_{rr} = {}^{\alpha}g_{22} = -e^{2\lambda(r^{\alpha})}, \\ {}^{\alpha}g_{\vartheta\vartheta} &= {}^{\alpha}g_{33} = -r^{2\alpha}, \quad {}^{\alpha}g_{\varphi\varphi} = {}^{\alpha}g_{44} = -r^{2\alpha}\sin^2\vartheta^{\alpha}. \end{aligned} \tag{10}$$

The fractional curvature tensor is defined in terms of fractional Christoffel symbols as follows:

$${}^{\alpha}R^{\lambda}_{\beta\mu\nu} = {}^{\alpha}\Gamma^{\lambda}_{\nu\beta,\mu} - {}^{\alpha}\Gamma^{\lambda}_{\mu\beta,\nu} + {}^{\alpha}\Gamma^{a}_{\beta\nu}{}^{\alpha}\Gamma^{\lambda}_{\mu a} - {}^{\alpha}\Gamma^{a}_{\mu\beta}{}^{\alpha}\Gamma^{\lambda}_{\nu a}, \tag{11}$$

since the comma subscript notation represents the coordinates fractional derivative, as, *i.e.*,

$${}^{\alpha}S_{,\mu} = \frac{\partial^{\alpha}S}{\partial x^{\mu a}}, \text{ or } {}^{\alpha}S_{,\mu} = D^{\alpha}_{\mu}S.$$

The fractional curvature at a point in space is fully represented by this fractional tensor, defined as

$${}^{\alpha}\Gamma^{\lambda}_{\mu\nu} = \frac{1}{2}{}^{\alpha}g^{\lambda a}({}^{\alpha}g_{a\nu,\mu} + {}^{\alpha}g_{a\mu,\nu} - {}^{\alpha}g_{\mu\nu,a}). \tag{12}$$

Note that

$$\begin{aligned} {}^{\alpha}g^{tt} &= {}^{\alpha}g^{11} = \frac{1}{e^{2\nu(r^{\alpha})}}, \quad {}^{\alpha}g^{rr} = {}^{\alpha}g^{22} = -\frac{1}{e^{2\lambda(r^{\alpha})}}, \\ {}^{\alpha}g^{\nu\nu} &= {}^{\alpha}g^{33} = -\frac{1}{r^{2\alpha}}, \quad {}^{\alpha}g^{\varphi\varphi} = {}^{\alpha}g^{44} = -\frac{1}{r^{2\alpha}\sin^2\vartheta^{\alpha}}, \end{aligned} \tag{13}$$

then we can calculate some of the fractional Christoffel symbols, ${}^{\alpha}\Gamma^{t}_{tt}$, ${}^{\alpha}\Gamma^{r}_{tt}$, ${}^{\alpha}\Gamma^{t}_{rt}$, ${}^{\alpha}\Gamma^{r}_{rr}$, ${}^{\alpha}\Gamma^{r}_{\vartheta\vartheta}$, ${}^{\alpha}\Gamma^{r}_{\varphi\varphi}$, ${}^{\alpha}\Gamma^{\theta}_{r\vartheta}$, ${}^{\alpha}\Gamma^{\phi}_{r\varphi}$, ${}^{\alpha}\Gamma^{\phi}_{\theta\varphi}$, and ${}^{\alpha}\Gamma^{\theta}_{\varphi\varphi}$.

The contracted fractional Riemann tensor, which is referred to as the fractional Ricci tensor, was obtained from the fractional Riemann tensor by contracting over two of the indices

$${}^{\alpha}R_{\mu\nu} \equiv {}^{\alpha}R^{k}_{\mu\nu k} = {}^{\alpha}\Gamma^{k}_{\mu\nu,k} - {}^{\alpha}\Gamma^{k}_{\nu k,\mu} + {}^{\alpha}\Gamma^{k}_{\mu\nu}{}^{\alpha}\Gamma^{m}_{km} - {}^{\alpha}\Gamma^{k}_{\mu m}{}^{\alpha}\Gamma^{m}_{\nu k}. \tag{14}$$

This fractional tensor is symmetric, so the Ricci scalar is then given by

$${}^{\alpha}R = {}^{\alpha}g^{\mu\nu}\ {}^{\alpha}R_{\mu\nu}. \tag{15}$$

In this fractional space-time, the fractional Einstein tensor ${}^{\alpha}G_{\mu\nu}$ can be formed by using the fractional metric tensor ${}^{\alpha}g_{\mu\nu}$, the fractional Ricci tensor ${}^{\alpha}R_{\mu\nu}$ and the fractional Ricci scalar ${}^{\alpha}R$ became

$${}^{\alpha}G_{\mu\nu} \equiv {}^{\alpha}R_{\mu\nu} - \frac{1}{2}{}^{\alpha}R{}^{\alpha}g_{\mu\nu} = \frac{8\pi G}{c^4}{}^{\alpha}T_{\mu\nu}, \tag{16}$$

where G is the gravitational acceleration, ${}^{\alpha}R_{\mu\nu}$ is known as the fractional Ricci tensor, ${}^{\alpha}R$ is the fractional Ricci scalar, ${}^{\alpha}g_{\mu\nu}$ is a fractional metric, c is the speed of light, and ${}^{\alpha}T_{\mu\nu}$ is the fractional stress-energy tensor, which contains all information about energy and matter in the space-time.

The fractional Christoffel symbols for spherically symmetric sources with coordinates $(ct,\ r,\ \nu,\ \varphi)$ are

$$\begin{aligned} &{}^{\alpha}\Gamma^{r}_{tt} = {}^{\alpha}\Gamma^{2}_{11} = e^{2(\nu-\lambda)}D^{\alpha}_{r}\nu, \quad {}^{\alpha}\Gamma^{t}_{tt} = {}^{\alpha}\Gamma^{1}_{11} = 0, \\ &{}^{\alpha}\Gamma^{t}_{rt} = {}^{\alpha}\Gamma^{1}_{21} = D^{\alpha}_{r}\nu, \quad {}^{\alpha}\Gamma^{r}_{rr} = {}^{\alpha}\Gamma^{2}_{22} = -D^{\alpha}_{r}\lambda, \\ &{}^{\alpha}\Gamma^{r}_{\vartheta\vartheta} = {}^{\alpha}\Gamma^{2}_{33} = -\alpha r^{\alpha}e^{-2\lambda}, \\ &{}^{\alpha}\Gamma^{r}_{\varphi\varphi} = {}^{\alpha}\Gamma^{2}_{44} = -\alpha r^{\alpha}\sin^2\vartheta^{\alpha}e^{-2\lambda}, \\ &{}^{\alpha}\Gamma^{\theta}_{r\vartheta} = {}^{\alpha}\Gamma^{3}_{23} = \frac{\alpha}{r^{\alpha}}, \quad {}^{\alpha}\Gamma^{\phi}_{r\varphi} = {}^{\alpha}\Gamma^{4}_{24} = \frac{\alpha}{r^{\alpha}}, \\ &{}^{\alpha}\Gamma^{\phi}_{\vartheta\varphi} = {}^{\alpha}\Gamma^{4}_{34} = \alpha\cot\vartheta^{\alpha}, \\ &{}^{\alpha}\Gamma^{\theta}_{\varphi\varphi} = {}^{\alpha}\Gamma^{3}_{44} = -2\alpha\sin\vartheta^{\alpha}\cos\vartheta^{\alpha}. \end{aligned} \tag{17}$$

Note that ${}^{\alpha}\Gamma^{\lambda}_{\mu\nu} = {}^{\alpha}\Gamma^{\lambda}_{\nu\mu}$. All unspecified symbols are zero or related by symmetry relations. Independent components can be calculated as the nonzero of the fractional Ricci tensor ${}^{\alpha}R_{\mu\nu}$ for a spherically symmetric source by using Eqs. (14) and (17)

$$
\begin{aligned}
{}^{\alpha}R_{tt} &= {}^{\alpha}R_{11} = \left(D_r^{\alpha\alpha}v - D_r^{\alpha}vD_r^{\alpha}\lambda + (D_r^{\alpha}v)^2 + \frac{2\alpha D_r^{\alpha}v}{r^{\alpha}}\right)e^{2(v-\lambda)},\\
{}^{\alpha}R_{\mu\nu} &= {}^{\alpha}R_{22} = D_r^{\alpha\alpha}v - D_r^{\alpha}vD_r^{\alpha}\lambda + (D_r^{\alpha}v)^2 + \frac{2\alpha D_r^{\alpha}\lambda}{r^{\alpha}},\\
{}^{\alpha}R_{\vartheta\vartheta} &= {}^{\alpha}R_{33} = (1 + ar^{\alpha}D_r^{\alpha}v - ar^{\alpha}D_r^{\alpha}\lambda)e^{-2\lambda} - 1,\\
{}^{\alpha}R_{\varphi\varphi} &= {}^{\alpha}R_{44} = {}^{\alpha}R_{22}\sin^2\varphi^{\alpha}.
\end{aligned}
\tag{18}
$$

The fractional scalar curvature in Eq. (15) is gained as a contraction of the fractional Ricci tensor with the fractional metric

$$
\begin{aligned}
{}^{\alpha}R = &-\frac{2e^{-2\lambda}}{r^{2\alpha}}(r^{2\alpha}D_r^{\alpha\alpha}v - r^{2\alpha}D_r^{\alpha}vD_r^{\alpha}\lambda + r^{2\alpha}(D_r^{\alpha}v)^2\\
&+ 2ar^{\alpha}D_r^{\alpha}v - 2ar^{\alpha}D_r^{\alpha}\lambda - e^{2\lambda} + 1).
\end{aligned}
\tag{19}
$$

The fractional Einstein's curvature tensor in Eq. (16) can now be obtained from the fractional Ricci tensor and the fractional scalar curvature

$${}^{\alpha}G_{(t)(t)} = \frac{e^{-2\lambda}}{r^{2\alpha}}(2ar^{\alpha}D_r^{\alpha}\lambda - 1) + \frac{1}{r^{2\alpha}} = \frac{8\pi G}{c^4}\rho(r^{\alpha})c^2, \tag{20}$$

$${}^{\alpha}G_{(r)(r)} = \frac{e^{-2\lambda}}{r^{2\alpha}}(1 + 2ar^{\alpha}D_r^{\alpha}v) - \frac{1}{r^{2\alpha}} = \frac{8\pi G}{c^4}p(r^{\alpha}), \tag{21}$$

$$
\begin{aligned}
{}^{\alpha}G_{(\vartheta)(\vartheta)} = e^{-2\lambda}&\left(D_r^{\alpha\alpha}v + (D_r^{\alpha}v)^2 - D_r^{\alpha}\lambda D_r^{\alpha}v + \frac{\alpha}{r^{\alpha}}(D_r^{\alpha}\lambda\right.\\
&\left. - D_r^{\alpha}v)\right) = \frac{8\pi G}{c^4}p(r^{\alpha}),
\end{aligned}
\tag{22}
$$

$${}^{\alpha}G_{(\varphi)(\varphi)} = {}^{\alpha}G_{(v)(v)}. \tag{23}$$

The fractional energy-momentum tensor is derived using a given stellar object's pressure and mass density. We will take the substance to be described by a perfect fluid at rest in the situation of a static, spherically symmetric fractional metric, such that

$${}^{\alpha}T^{\mu\nu} = \rho(r^{\alpha}){}^{\alpha}u^{\mu}\,{}^{\alpha}u^{\nu} + \frac{p(r^{\alpha})}{c^2}({}^{\alpha}u^{\mu}\,{}^{\alpha}u^{\nu} - {}^{\alpha}g^{\mu\nu}), \tag{24}$$

since $\rho(r^{\alpha})$ is the proper mass density and $p(r^{\alpha})$ is the isotropic pressure in the instantaneous rest frame of the fluid, both of which may be given as functions only of the radial coordinate r^{α} for a static matter distribution, and ${}^{\alpha}u^{\mu}$ the fractional velocity vector.

By the law of local fractional energy-momentum conservation $D_v^{\alpha}\,{}^{\alpha}T^{\mu\nu} = 0$, the r-component of this conservation law is

$$(\rho c^2 + p)D_r^{\alpha}v = -D_r^{\alpha}p. \tag{25}$$

The comfortable fractional hydrostatic equilibrium equation describes the balance between the fractional gravitational force and the fractional pressure gradient. First, we shall discuss the $(t)(t)$ component that is

$${}^{\alpha}G_{(t)(t)} = \frac{e^{-2\lambda}}{r^{2\alpha}}(2ar^{\alpha}D_r^{\alpha}\lambda - 1) + \frac{1}{r^{2\alpha}} = \frac{8\pi G}{c^4}\rho(r^{\alpha})c^2, \tag{26}$$

this can be transferred into the form

$$D_r^{\alpha}(r^{\alpha}(1 - e^{-2\lambda}) = D_r^{\alpha}\left(\frac{2\alpha G}{c^2}m\right). \tag{27}$$

Performing the conformable fractional integration to Eq. (27), we have

$$e^{2\lambda} = r^{\alpha}\left[r^{\alpha} - \frac{2\alpha Gm}{c^2}\right]^{-1}. \tag{28}$$

The $(r)(r)$ component (Eq. (21)) of the field equations reads

$${}^{\alpha}G_{(r)(r)} = \frac{e^{-2\lambda}}{r^{2\alpha}}\left(1 + \frac{2r^{\alpha}}{\alpha}D_r^{\alpha}v\right) - \frac{1}{r^{2\alpha}} = \frac{8\pi G}{c^4}p(r^{\alpha}), \tag{29}$$

then we obtain

$$D_r^{\alpha}v = \frac{\frac{\alpha G}{c^2}m + \frac{4\pi G}{c^4}pr^{3\alpha}}{\frac{r^{\alpha}}{\alpha}\left[r^{\alpha} - \frac{2\alpha G}{c^2}m\right]}, \tag{30}$$

which enables us to put the fractional equation of hydrostatic equilibrium into the fractional Tolman–Oppenheimer–Volko (TOV) form as

$$D_r^{\alpha}p = -(\rho c^2 + p)\frac{\frac{2\alpha G}{c^2}m + \frac{4\pi G}{c^4}pr^{3\alpha}}{\frac{2r^{\alpha}}{\alpha}\left[r^{\alpha} - \frac{2\alpha G}{c^2}m\right]}, \tag{31}$$

in another form

$$D_r^{\alpha}p = -\frac{Gm\rho}{r^{2\alpha}}\left[1 + \frac{p}{c^2\rho}\right]\left[1 + \frac{8\pi r^{3\alpha}p}{2\alpha c^2 m}\right]\left[1 - \frac{2\alpha Gm}{c^2r^{\alpha}}\right]^{-1}, \tag{32}$$

where G is the Newtonian gravitational constant. Eq. (32) is the fractional TOV (FTOV) equation that defines the fractional relativistic hydrostatic equilibrium of the static isotropic fluid sphere. This equation provides the equilibrium pressure solution for a compact star when combined with the mass, Eq. (28), and a microscopic explanation for the pressure-energy density connection.

The relation between the energy density and pressure of the fluid given by the isothermal polytropic equation of state is

$$p(r^{\alpha}) = K\rho(r^{\alpha}), \tag{33}$$

$$\rho(r^{\alpha}) = \rho_c e^{-\theta}, \tag{34}$$

$$D_r^{\alpha}p = -\alpha K\rho_c e^{-\theta}D_r^{\alpha}\theta, \tag{35}$$

where K is the Boltzmann constant. The mass density is a function of temperature for a given pressure and K

includes the temperature implicitly. It can be proved that K is dictated by the radius, total mass, and $p_c/\rho_c c^2$ ratio. Since

$$(\rho c^2 + p)D_r^\alpha v = -D_r^\alpha p, \tag{36}$$

then

$$-\alpha\frac{K\rho_c e^{-\theta}}{c^2}D_r^\alpha\theta + \left(\frac{K\rho_c e^{-\theta}}{c^2} + \rho_c\right)D_r^\alpha v = 0, \tag{37}$$

with $\sigma = K/c^2$, Eq. (37) could be written as

$$-\alpha\,\sigma D_r^\alpha\theta + (1 + \sigma e^{-\theta})D_r^\alpha v = 0. \tag{38}$$

We obtain from Eq. (21) that

$$\frac{e^{-2\lambda}}{r^{2\alpha}}\left(1 + \frac{2r^\alpha}{\alpha}D_r^\alpha v\right) - \frac{1}{r^{2\alpha}} = \frac{8\pi G}{c^4}p, \tag{39}$$

or

$$\frac{1}{r^{2\alpha}}\left(1 - \frac{2\alpha G m(r^\alpha)}{r^\alpha c^2}\right)\left(1 + \frac{2r^\alpha}{\alpha}D_r^\alpha v\right) - \frac{1}{r^{2\alpha}} = \frac{8\pi G}{c^4}p. \tag{40}$$

Substituting Eqs. (33) and (34) in Eq. (40), we obtain

$$\begin{aligned}\xi^{2\alpha}D_\xi^\alpha\theta - \frac{2\alpha\sigma(n+1)(1+\sigma\theta)AGm}{c^2\sigma(n+1)(1+\sigma\theta)}\xi^\alpha D_\xi^\alpha\theta \\ - \frac{(1+\sigma\theta)GmA}{\sigma(1+n)c^2} - \frac{8\pi G(1+\sigma\theta)}{2\alpha\sigma(1+n)c^4A^2}\sigma\theta\rho\xi^{3\alpha} = 0,\end{aligned} \tag{41}$$

where

$$\xi = rA, \tag{42}$$

$$A = \left(\frac{8\pi G\rho_c}{2\alpha\sigma c^2}\right)^{1/2}, \tag{43}$$

and the mass function is given by

$$\upsilon(\xi) = \frac{m(r^\alpha)}{M} = \frac{GAm(r^\alpha)}{2\alpha\sigma c^2}. \tag{44}$$

Then, the fractional TOV Eqs (FTOVI) have the form

$$\begin{aligned}\xi^{2\alpha}D_\xi^\alpha\theta - 2\alpha\sigma(n+1)\xi^\alpha\upsilon D_\xi^\alpha\theta + \upsilon + \upsilon\sigma\theta + \sigma\xi^\alpha\theta D_\xi^\alpha\upsilon \\ + \sigma^2\xi^\alpha\theta^2 D_\xi^\alpha\upsilon = 0,\end{aligned} \tag{45}$$

and

$$D_\xi^\alpha\upsilon = \xi^{2\alpha}\theta^n, \tag{46}$$

with the initial conditions

$$\theta(0) = 1, \quad \upsilon(0) = 0, \quad D_\xi^{\alpha\alpha}\theta = D_\xi^\alpha(D_\xi^\alpha\theta). \tag{47}$$

4 Series solution of FTOVI

4.1 Successive fractional derivative of the Emden function

To solve the FTOVI equations, Eqs. (45) and (46), we consider a series expansion as

$$\begin{aligned}\theta(\xi) &= \sum_{m=0}^{\infty} A_m\xi^m, \\ \theta(\xi) &= A_0 + A_1\xi + A_2\xi^3 + A_3\xi^3 + ...\end{aligned} \tag{48}$$

We can rewrite Eq. (48) in the fractional form as

$$\theta(\xi^\alpha) = A_0 + A_1\xi^\alpha + A_2\xi^{2\alpha} + A_3\xi^{3\alpha} + ... \tag{49}$$

At $\theta(0) = 0, \quad A_0 = 0,$
then

$$\theta(\xi^\alpha) = \sum_{m=1}^{\infty} A_m\xi^{2\alpha m}. \tag{50}$$

Applying the fractional derivative to Eq. (50) gives

$$D_\xi^\alpha\theta = \sum_{m=0}^{\infty}\alpha m A_m\xi^{\alpha m-\alpha}, \tag{51}$$

$$\begin{aligned}D_\xi^\alpha\theta &= \alpha A_1 + 2\alpha A_2\xi^\alpha + 3\alpha A_3\xi^{2\alpha} + 4\alpha A_4\xi^{3\alpha}... \\ &= \sum_{m=1}^{\infty}\alpha m A_m\xi^{\alpha m-\alpha}, \\ D_\xi^{\alpha\alpha}\theta &= 2\alpha^2A_2 + 6\alpha^2A_3\xi^\alpha + 12\alpha^2A_4\xi^{2\alpha} + 20\alpha^2A_5\xi^{3\alpha}... \\ &= \sum_{m=2}^{\infty}\alpha^2 m(m-1)A_m\xi^{\alpha m-2\alpha}.\end{aligned} \tag{52}$$

Applying the second initial condition $D_\xi^\alpha\theta(0) = 0,$ gives $\alpha A_1 = 0$, this gives $A_1 = 0$. Then, the differential j time where $j = 1, 2, 3,...$ time to be

$$D_\xi^{\overbrace{\alpha...\alpha}^{j\text{ times}}}\theta(\xi^\alpha) = \sum_{m=j}^{\infty}A_m\alpha^j m(m-1)...(m-j+1)\xi^{\alpha m-j\alpha},$$

at $X(\xi^\alpha) = 0,$
then

$$\begin{aligned}D_\xi^{\overbrace{\alpha...\alpha}^{j\text{ times}}}\theta(0) &= j!A_j\alpha^j, \\ D_\xi^{\alpha\alpha}\theta(0) &= 2!A_2\alpha^2,\end{aligned} \tag{53}$$

where A_j are the constants to be determined.

4.2 Fractional derivative of the Emden function raised to powers

Now, we suppose that

$$e^{-\theta} = \sum_{m=0}^{\infty} Q_m \xi^m = G(\xi), \quad G(0) = 1,$$

this gives $Q_0 = 1$. Now, let

$$\begin{aligned} e^{-\theta} &= \sum_{m=0}^{\infty} Q_m \xi^{\alpha m} = G(\xi^\alpha), \\ e^{-\theta} &= Q_0 + Q_1\xi^\alpha + Q_2\xi^{2\alpha} + Q_3\xi^{3\alpha} + Q_4\xi^{4\alpha} + \ldots, \end{aligned} \tag{54}$$

since

$$D_\xi^\alpha G = -G D_\xi^\alpha \theta. \tag{55}$$

Differentiating both sides of Eq. (54) k times α-derivatives, we have

$$\overbrace{D_\xi^\alpha \ldots D_\xi^\alpha}^{k-\text{times}}[G D_\xi^\alpha \theta] = -\overbrace{D_\xi^\alpha \ldots D_\xi^\alpha}^{k-\text{times}} D_\xi^\alpha G, \tag{56}$$

or

$$\sum_{j=0}^{k} \binom{k}{j} \theta^{\overbrace{\alpha\ldots\alpha}^{j+1}} G^{\overbrace{\alpha\ldots\alpha}^{k-j}} = -G^{\overbrace{\alpha\ldots\alpha}^{k+1}}. \tag{57}$$

At $\xi = 0$, we have

$$\sum_{j=0}^{k} \binom{k}{j} \theta^{\overbrace{\alpha\ldots\alpha}^{j+1}}(0) G^{\overbrace{\alpha\ldots\alpha}^{k-j}}(0) = -G^{\overbrace{\alpha\ldots\alpha}^{k+1}}(0), \tag{58}$$

since

$$\theta^{\overbrace{\alpha\ldots\alpha}^{j+1}}(0) = (j+1)! A_{j+1}\alpha^{j+1}, \quad G^{\overbrace{\alpha\ldots\alpha}^{k-j}}(0) = (k-j)! Q_{k-j}\alpha^{k-j},$$

$$G^{\overbrace{\alpha\ldots\alpha}^{k+1}}(0) = (k+1)! Q_{k+1}\alpha^{k+1},$$

we have

$$\sum_{j=0}^{k} \binom{k}{j} (j+1)! A_{j+1}\alpha^{j+1}(k-j)! Q_{k-j}\alpha^{k-j} = -(k+1)! Q_{k+1}\alpha^{k+1},$$

this gives

$$\begin{aligned} Q_{k+1} &= -\frac{1}{(k+1)!}\sum_{j=0}^{k} \frac{k!(j+1)! A_{j+1}(k-j)! Q_{k-j}}{j!(k-j)!} \\ &= -\frac{1}{k+1}\sum_{j=0}^{k}(j+1)A_{j+1}Q_{k-j}, \end{aligned}$$

let

$$l = k+1,$$

then

$$Q_l = -\frac{1}{l}\sum_{j=0}^{l-1}(j+1)A_{j+1}Q_{l-j-1}, \tag{59}$$

where

$$A_0 = 0, \quad A_1 = 0, \quad Q_0 = 1, \quad Q_1 = 0, \quad Q_2 = -A_2 Q_0.$$

4.3 Fractional derivative of series expansion of the relativistic function

From Eq. (51), we obtain

$$D_\xi^\alpha \theta = \sum_{m=0}^{\infty} U_{m+1}A_{m+1}\xi^{\alpha m}, \quad U_{m+1} = \alpha(m+1),$$

then

$$\xi^{2\alpha} D_\xi^\alpha \theta = \sum_{m=0}^{\infty} U_{m+1}A_{m+1}\xi^{\alpha m + 2\alpha}, \tag{60}$$

where $D_\xi^\alpha \upsilon = \xi^{2\alpha} e^{-\theta} = \sum_{m=0}^{\infty} Q_m \xi^{\alpha m + 2\alpha}$, then

$$\upsilon = \sum_{m=0}^{\infty} \frac{1}{\alpha m + 3\alpha} Q_m \xi^{\alpha m + 3\alpha},$$

$$\upsilon = \sum_{m=0}^{\infty} N_m \xi^{\alpha m + 3\alpha}, \tag{61}$$

where

$$N_m = \frac{1}{\alpha m + 3\alpha} Q_m, \tag{62}$$

by using Eqs. (60) and (61), we obtain

$$\xi^\alpha \upsilon D_\xi^\alpha \theta = \left(\sum_{m=0}^{\infty} U_{m+1}A_{m+1}\xi^{\alpha m + \alpha}\right)\left(\sum_{m=0}^{\infty} N_m \xi^{\alpha m + 3\alpha}\right),$$

where

$$f_m = A_{m+1}U_{m+1},$$

then

$$\begin{aligned} \xi^\alpha \upsilon D_\xi^\alpha \theta &= \left(\sum_{m=0}^{\infty} f_m \xi^{\alpha m + \alpha}\right)\left(\sum_{m=0}^{\infty} N_m \xi^{\alpha m + 3\alpha}\right) \\ &= (f_0\xi^\alpha + f_1\xi^{2\alpha} + f_2\xi^{3\alpha} + \ldots)(N_0\xi^{3\alpha} + N_1\xi^{4\alpha} + N_2\xi^{5\alpha} + \ldots) \\ &= N_0 f_0 \xi^{4\alpha} + (N_0 f_1 + N_1 f_0)\xi^{5\alpha} + (N_0 f_2 + N_1 f_1 + N_2 f_0)\xi^{6\alpha} \\ &= \sum_{m=0}^{\infty} \gamma_m \xi^{\alpha m + 3\alpha}, \end{aligned}$$

where

$$\begin{aligned} \gamma_m &= \sum_{i=0}^{m} f_i N_{m-i}, \\ f_i &= A_{i+1}U_{i+1}. \end{aligned} \tag{63}$$

By using Eq. (54), we obtain

$$e^{-\theta}\xi^{3\alpha} = \sum_{m=0}^{\infty} Q_m \xi^{\alpha m+3\alpha}. \tag{64}$$

4.4 Recurrence relations

Substituting Eqs. (61–64) in Eq. (46), we obtain

$$\begin{aligned}&\sum_{m=0}^{\infty} U_{m+1}A_{m+1}\xi^{\alpha m+2\alpha} - 2\alpha\sigma\sum_{m=0}^{\infty}\gamma_m\xi^{\alpha m+3\alpha} - \sum_{m=0}^{\infty} N_m\xi^{\alpha m+3\alpha}\\ &- \sigma\sum_{m=0}^{\infty} N_m\xi^{\alpha m+3\alpha} - \sigma\sum_{m=0}^{\infty} Q_m\xi^{\alpha m+3\alpha} - \sigma^2\sum_{m=0}^{\infty} Q_m\xi^{\alpha m+3\alpha}\\ &= 0.\end{aligned} \tag{65}$$

We can rewrite this equation in the like power of ξ, we have

$$\begin{aligned}&U_{m+2}A_{m+2} - 2\alpha\sigma\gamma_m - N_m - \sigma N_m - \sigma Q_m - \sigma^2 Q_m = 0,\\ &\gamma_m = \sum_{i=0}^{m} f_i N_{m-i}.\end{aligned} \tag{66}$$

Now, we obtain

$$A_{m+2} = \frac{\sigma}{U_{m+2}}(2\alpha\gamma_m + N_m + Q_m + \sigma Q_m) + \frac{N_m}{U_{m+2}}, \tag{67}$$

where

$$A_0 = 0, \quad A_1 = 0, \quad Q_0 = 1, \quad Q_1 = 0.$$

By applying the initial condition in Eq. (67) when $m = 0$, we obtain

$$A_2 = \frac{\sigma}{U_2}(N_0 + Q_0 + \sigma Q_0) + \frac{N_0}{U_2},$$

where

$$f_0 = A_1U_1, \quad N_0 = \frac{1}{3\alpha}Q_0, \quad U_2 = 2\alpha.$$

If we put $\alpha = 1$, the series coefficients will be reduced to the integer case, *i.e.*,

$$A_2 = \frac{1}{6}(1+\sigma)(1+3\sigma),$$

where $f_0 = 2$, $N_0 = \frac{1}{3}$, $U_1 = 2$ at $\sigma = 0$, then obtain the series coefficients of the integer Newtonian case as

$$A_2 = \frac{1}{6}.$$

It has been observed that the series solution of the Emden function remains valid for small values of ξ; however, beyond that range, the series begins to diverge [32,33]. Divergent or slowly converging series are common in the physical sciences, and various approaches have been proposed to address this challenge. Nouh *et al.* [33,34] tackled this problem by combining two different transforms. Specifically, the series is accelerated using the Euler-Abel transformation [35] before being approximated by the Padé technique.

5 Analysis of the numerical results

The complete configuration of the FRISG occurs at $\xi_1 \approx 35$ [32]; this means that we try to obtain the analytical solution from $\xi = 0$ (at the center) to $\xi_1 = 35$ (at the surface) along the radius of the sphere. We employed power series expansions to solve the FTOVI equation, deriving an analytical solution from the center to the sphere's surface. This analytical solution, based on the specified initial conditions, characterizes the fractional relativistic structure of the configuration and is expressed in Eqs. (59) and (61), along with Eqs. (59)–(67). For the fractional parameter $\alpha = 1$, the series solution of the FTOVI reduces to the series solution of the conformable isothermal gas sphere as presented by Yousif *et al.* [23]. The numerical comparison between the Emden functions derived from the series solution and those obtained using the Runge-Kutta method shows good agreement for dimensionless parameters up to approximately $\xi \simeq 3.2$; beyond this value, the series diverges. Consequently, it became essential to enhance the power series solution of the FTOVI equation, which, in turn, improved the approximation of the physical parameters of stars. To accelerate the convergence of the series, we adopted the method implemented by Nouh *et al.* [33,34], combining the Euler-Abel transformation and Padé approximation while following the calculation procedure. Figure 1 displays the Emden function (θ) calculated for the relativistic parameter $\sigma = 0.1$ and the fractional parameters $\alpha = 0.95$; as is clear, the original series (without acceleration) diverges (the red curve), whereas the series accelerated by Euler-Abel transformation and Padé approximation (the blue curve) converges to the desired value.

The inputs to the Mathematica code are the fractional parameters (α), the relativistic parameter (σ), the number of terms in the original series (m), and the central density (ρ_c). The outputs of the code are the Emden function (θ), the fractional first derivative of the Emden function (θ'), the mass function (υ), the density profile (ρ), the pressure profile (P), and the mass ($M(r)$). To analyze the physical properties of the models, we first calculated models for a range of the relativistic parameter $\sigma = 0 - 0.5$ with step $\Delta\sigma = 0.05$, and the range of the fractional parameter $\alpha = 0.95 - 1$ with step $\Delta\alpha = 0.01$.

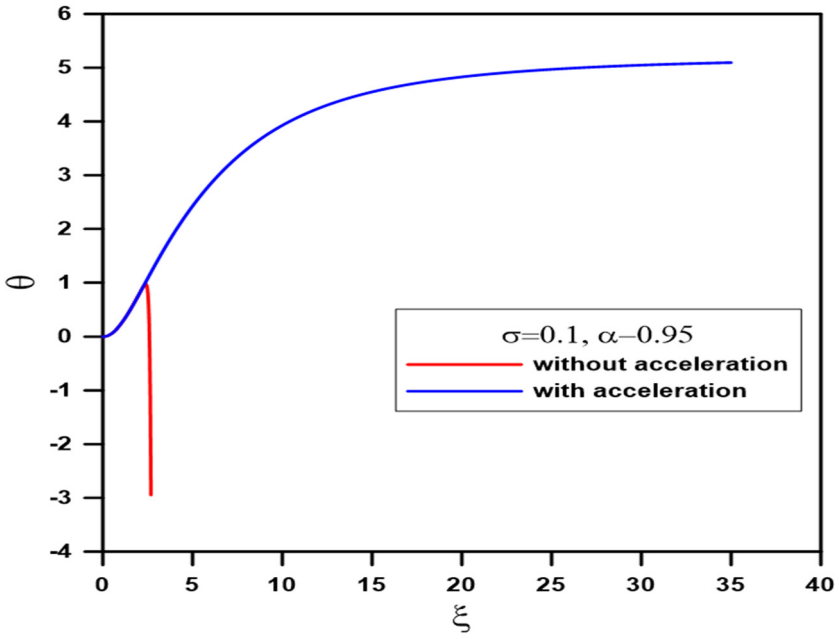

Figure 1: The Emden function of the FRISG with σ = 0.1, α = 0.95. The red line represents the function before series acceleration, while the blue line represents the function after series acceleration.

Tables 1–3 present the Emden function (θ), the mass function υ, and the first derivative of the Emden function θ' across various values of the relativistic parameters σ and fractional parameters α. These functions are calculated at the zero (ξ_1 = 35) of the FRISG. The Emden function θ rises as σ increases, which means that the enhanced relativistic effect (or stronger gravitational effects) leads to a faster increase in density as one advances away from the center of the sphere. As α decreases from 1 to 0.95, θ usually decreases, suggesting that smaller fractional values are associated with a slower decline in the Emden function, which likely indicates a more compact structure. The mass function υ tends to decrease as σ increases, suggesting that the mass contained inside a specific radius ξ_1 is bigger for higher relativistic effects. This might be due to the greater sphere compression under higher gravity. A drop in α tends to increase υ as well, implying that the mass distribution is denser or more stretched for spheres with lower fractional values. The value of θ tends to decrease more as σ rises, suggesting a steeper gradient in the Emden function,

Table 1: Emden function θ (ξ_1), the mass function υ (ξ_1), and the first derivative of the Emden function θ'(ξ_1) for the fractional isothermal gas sphere for α = 1 and 0.99

σ	α = 1			α = 0.99		
	θ (ξ_1)	υ (ξ_1)	θ' (ξ_1)	θ (ξ_1)	υ (ξ_1)	θ' (ξ_1)
0	5.217	74.437	0.0630	5.217	74.437	0.0630
0.05	5.075	64.002	0.0546	5.075	64.002	0.0546
0.1	5.086	57.902	0.0418	5.086	57.902	0.0418
0.15	5.182	54.948	0.0753	5.182	54.948	0.0753
0.2	5.333	52.577	0.0812	5.333	52.577	0.0812
0.25	5.521	50.072	0.0866	5.521	50.072	0.0866
0.3	5.729	47.657	0.0913	5.729	47.657	0.0913
0.35	5.944	45.503	0.0954	5.944	45.503	0.0954
0.4	6.158	43.658	0.0991	6.158	43.658	0.0991
0.45	6.364	42.103	0.1024	6.364	42.103	0.1024
0.5	6.558	40.794	0.1053	6.558	40.794	0.1053

Table 2: Emden function θ (ξ_1), the mass function υ (ξ_1), and the first derivative of the Emden function θ' (ξ_1) for the fractional isothermal gas sphere for α = 0.98 and 0.97

σ	α = 0.98			α = 0.97		
	θ (ξ_1)	υ (ξ_1)	θ' (ξ_1)	θ (ξ_1)	υ (ξ_1)	θ' (ξ_1)
0	5.205	71.235	0.0647	5.193	68.168	0.0666
0.05	5.066	61.377	0.0565	5.057	58.850	0.0585
0.1	5.077	55.502	0.0706	5.069	53.196	0.0465
0.15	5.172	52.546	0.0767	5.161	50.247	0.0781
0.2	5.321	50.211	0.0826	5.308	47.949	0.0840
0.25	5.506	47.779	0.0879	5.491	45.591	0.0893
0.3	5.712	45.438	0.0927	5.695	43.323	0.0941
0.35	5.926	43.343	0.0968	5.907	41.287	0.0983
0.4	6.139	41.539	0.1005	6.119	39.528	0.1020
0.45	6.344	40.012	0.1038	6.324	38.030	0.1053
0.5	6.538	38.719	0.1068	6.517	36.745	0.1084

Table 3: Emden function θ (ξ_1), the mass function υ (ξ_1), and the first derivative of the Emden function θ' (ξ_1) for the fractional isothermal gas sphere for α = 0.96 and 0.95

σ	α = 0.96			α = 0.95		
	θ (ξ_1)	υ (ξ_1)	θ' (ξ_1)	θ (ξ_1)	υ (ξ_1)	θ' (ξ_1)
0	5.179	65.229	0.0684	5.166	62.414	0.0704
0.05	5.048	56.417	0.0606	5.038	54.077	0.0627
0.1	5.059	50.980	0.0737	5.050	48.850	0.0740
0.15	5.150	48.046	0.0796	5.139	45.939	0.0784
0.2	5.295	45.788	0.0854	5.282	43.722	0.0831
0.25	5.476	43.501	0.0907	5.460	41.506	0.0880
0.3	5.677	41.307	0.0955	5.659	39.384	0.0927
0.35	5.887	39.332	0.0997	5.868	37.470	0.0972
0.4	6.098	37.617	0.1035	6.077	35.801	0.1014
0.45	6.302	36.151	0.1069	6.281	34.369	0.1052
0.5	6.496	34.899	0.1099	6.474	33.141	0.1088

corresponding with a more steeply falling density profile. Lower α values also lead to smaller θ values, which correspond to steeper profiles.

Figures 2–4 represent the solution curves of the FTOVI equation in $\xi - \theta$, $\xi - \theta'$, and $\xi - \upsilon$, respectively. The fractional parameter has a value of α = 0.99 and the general relativistic parameter has a range $\sigma = 0 - 0.5$ with steps $\Delta\sigma = 0.05$. The curves in Figure 1 show the behavior of the Emden function ($\theta(\xi)$) for different values of σ, with the fractional parameter α = 1, 0.99, 0.95. Each curve rises quickly as ξ increases, beginning at ($\xi = 0$, $\theta = 0$). This initial fast climb demonstrates that the Emden function gains value quickly when the radial coordinate increases from 0. Each curve rises first, then flattens to a plateau when the function θ approaches a constant value. As ξ increases, the system moves closer to equilibrium. The plateau's height is determined by the value of the relativistic parameter (σ). The curves are closely spaced, particularly at smaller σ values, demonstrating that the dependency of the Emden function on σ increases with σ. Every curve ultimately saturates, which means that after a certain ξ, θ does not increase much. The predicted physical behavior of these gas spheres is consistent with the smooth, monotonic curves free of oscillations and abrupt shifts. These characteristics demonstrate the fluctuating nature of the Emden function $\theta(\xi)$ due to the fractional parameter α and σ. So, it is clear that, σ is an important parameter in determining the form and height of the curves.

Figure 2 displays the Emden function's fractional first derivative (θ'). The non-relativistic situation is represented by the curve for $\sigma = 0$, and the curves for $\sigma > 0$ represent the relativistic case. The curves get peaked and tilted to the right as the relativistic parameter σ rises. This suggests that as the relativistic effects increase in strength, the fractional first derivative of the Emden function concentrates closer to the sphere's surface and diminishes more slowly with increasing radius. The fractional derivative at α = 0.99 is near the classical first derivative, consequently, the graph's curves resemble the curves that would be obtained for the traditional first derivative in terms of quality, while for α = 0.95, the change is remarkable. The fractional derivative adds more characteristics, such as slower decay at large radii and smoother behavior close to the origin. Overall, the graph indicates that the relativistic parameter σ considerably affects the fractional first derivative of the Emden function. As σ increases, the curves are more peaked and pushed to the right, suggesting that θ' is concentrated closer to the sphere's surface and drops more slowly as the radius increases.

The mass function is displayed in Figure 3. The curves get steeper and attain a larger maximum value at a smaller radius as the relativistic parameter σ increases; this suggests that when the relativistic effects intensify, the sphere's mass concentrates closer to the center. Although the deviation is small for the model with α = 0.99 from the integer case, the fractional derivative adds more characteristics, such as a slower decay at large radii and a smoother behavior close to the origin; this deviation becomes larger for the model with α = 0.95. Also, the graph indicates that the relativistic parameter σ considerably impacts the mass function, as σ increases, the curves get steeper and attain a smaller maximum value at a smaller radius, suggesting that the star's mass is more compacted and concentrated on the core.

Now, we shall investigate the effects of varying the fractional parameter (α) on the FRISG. Figure 5 shows the Emden function, the first fractional derivative of the Emden function, and the mass function. The calculations used fractional parameters α = 0.95–1 and relativistic parameters σ = 0.1 and 0.3.

The Emden function is shown with different colors calculated at different fractional parameter α values in the top panel of Figure 5. The curves for $\alpha < 1$ and $\alpha = 1$ depict the fractional and integer Emden functions, respectively. As α decreases, the curves flatten and reach a smaller maximum value at larger radii. This behavior shows that the gas sphere's density expands as the fractional parameter declines, reducing its central concentration. The moderate relativistic parameter σ = 0.1 shows that the relativistic effects are of small size (consequently, the curves illustrated in the graph display a similar qualitative resemblance to those generated in the non-relativistic case [23]), while the size of the effect increases and is clearer at σ = 0.3.

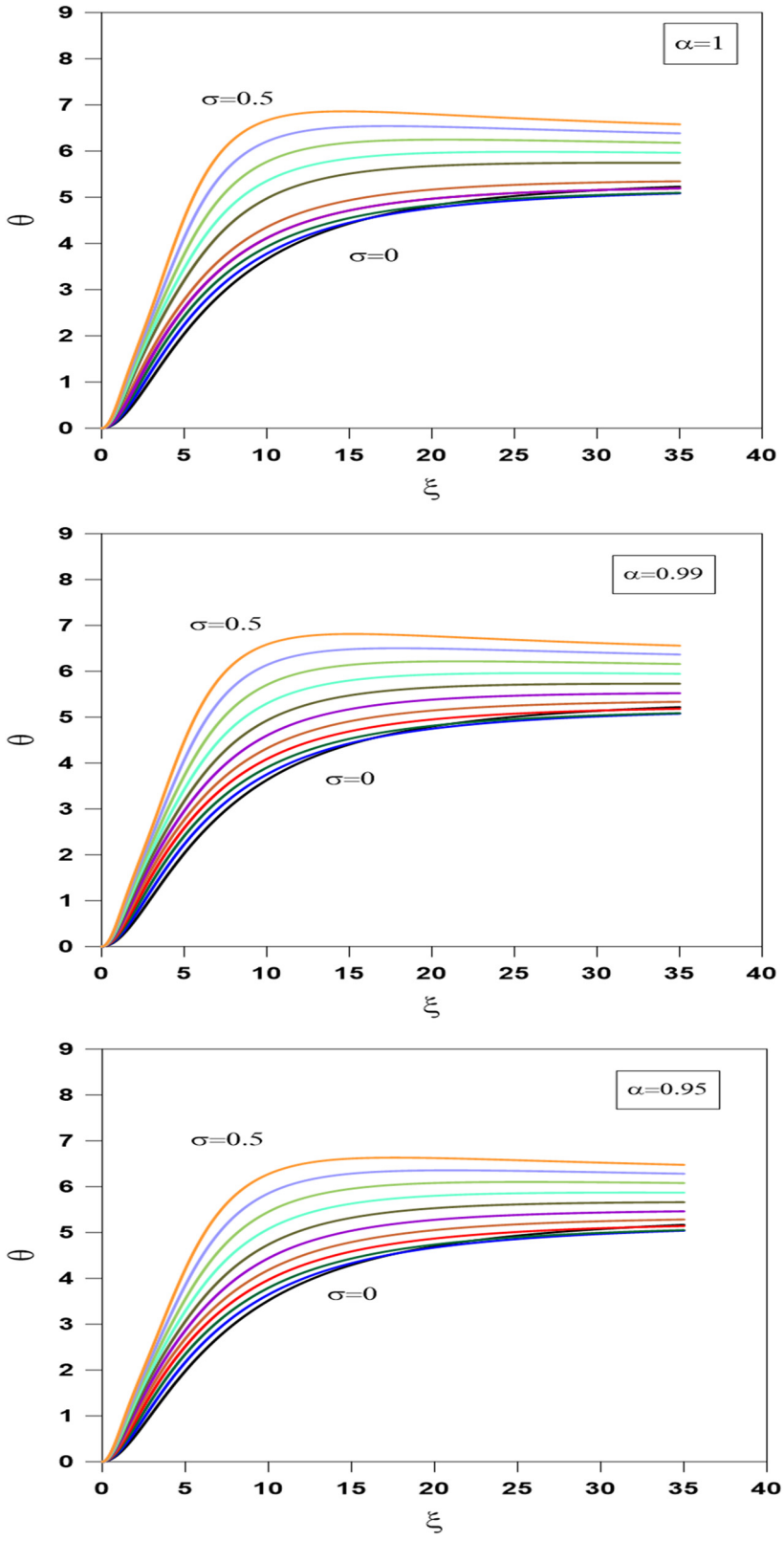

Figure 2: The Emden function (θ) of the FRISG. The relativistic parameter varies from 0 to 0.5, while the fractional parameter is α = 1 (top panel), α = 0.99 (central panel), and α = 0.95 (bottom panel).

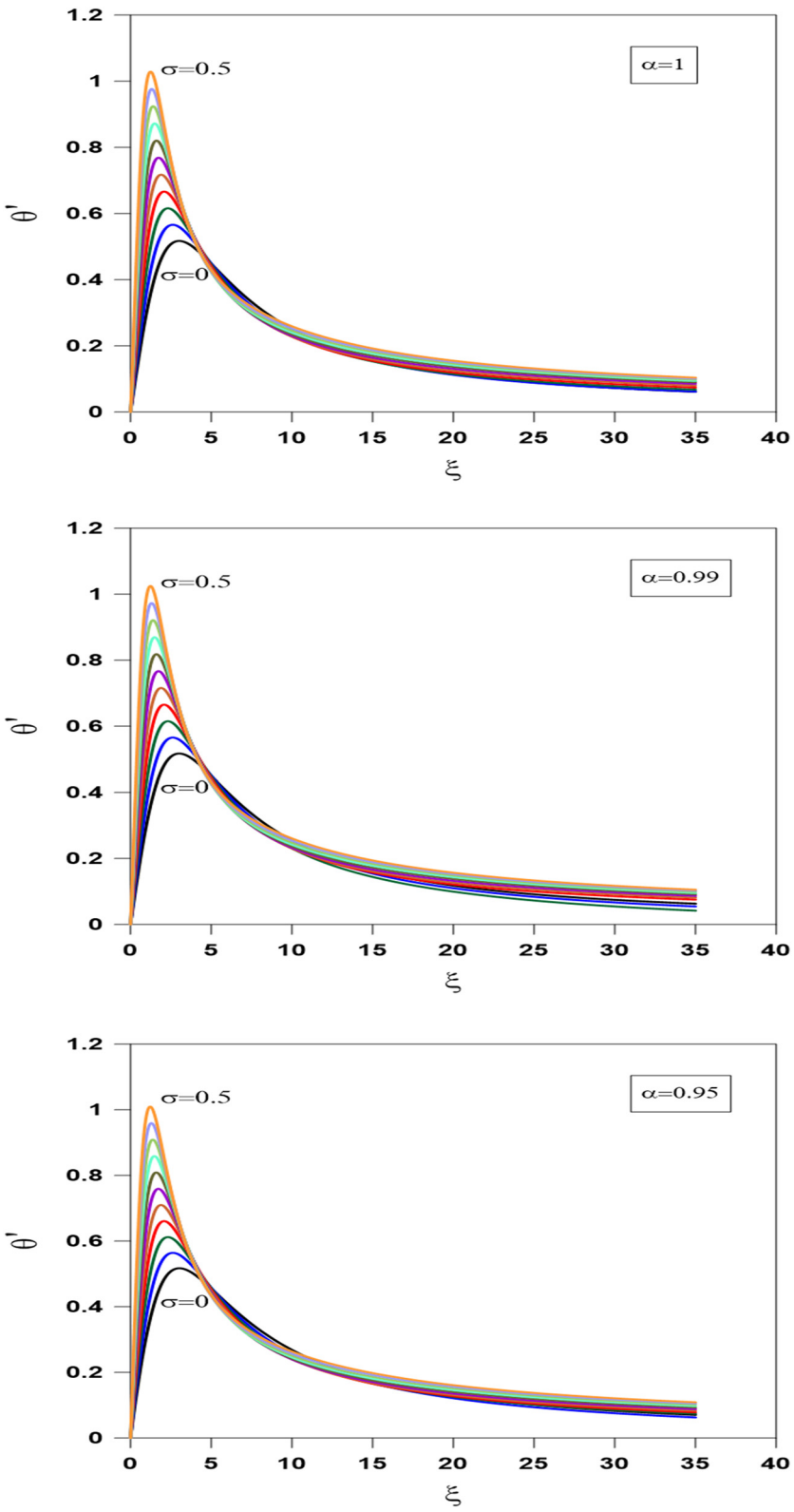

Figure 3: The first fractional derivative of the Emden function (θ') of the FRISG. The relativistic parameter varies from 0 to 0.5, while the fractional parameter is α = 1 (top panel), α = 0.99 (central panel), and α = 0.95 (bottom panel).

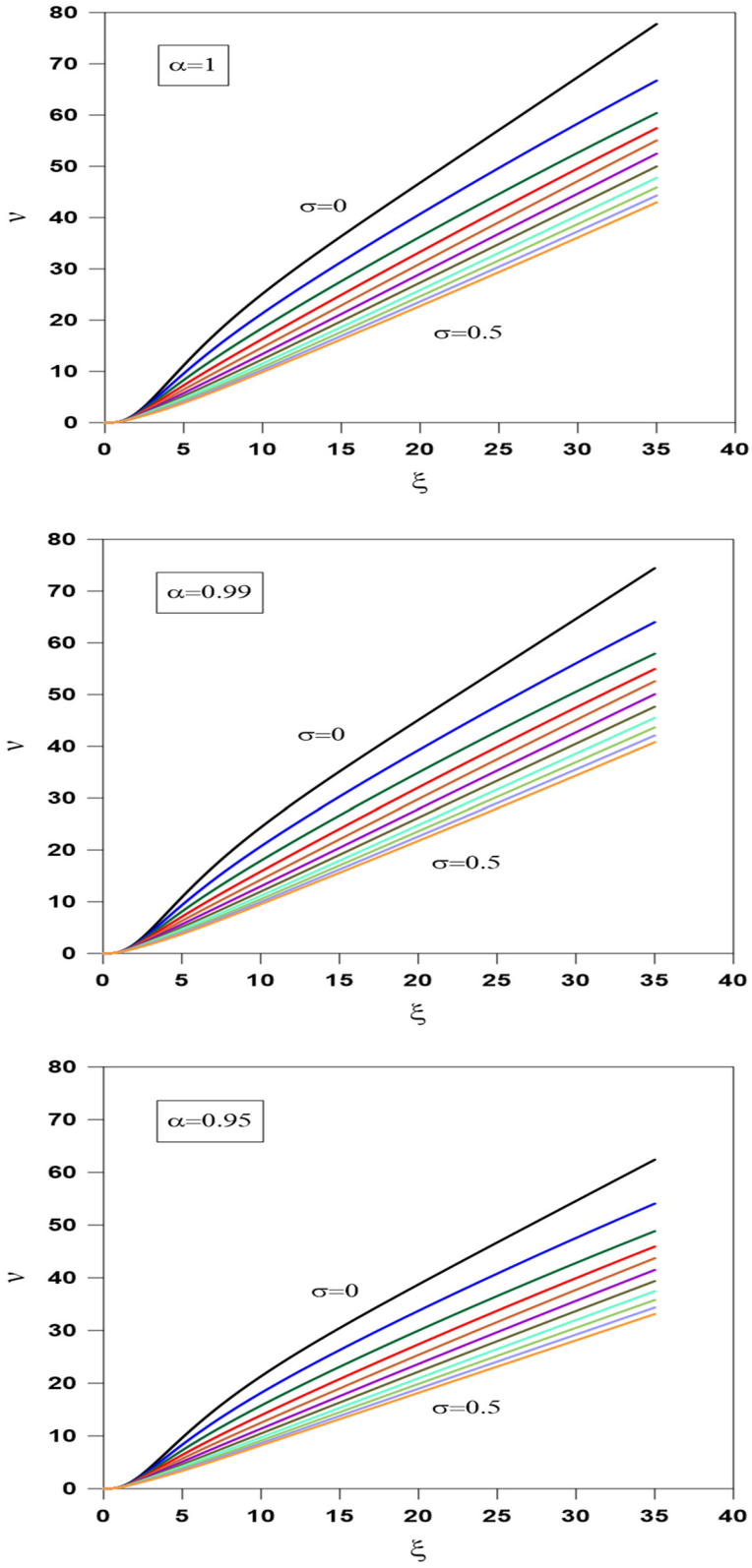

Figure 4: The mass function (υ) of the FRISG. The relativistic parameter varies from 0 to 0.5, while the fractional parameter is $\alpha = 1$ (top panel), $\alpha = 0.99$ (central panel), and $\alpha = 0.95$ (bottom panel).

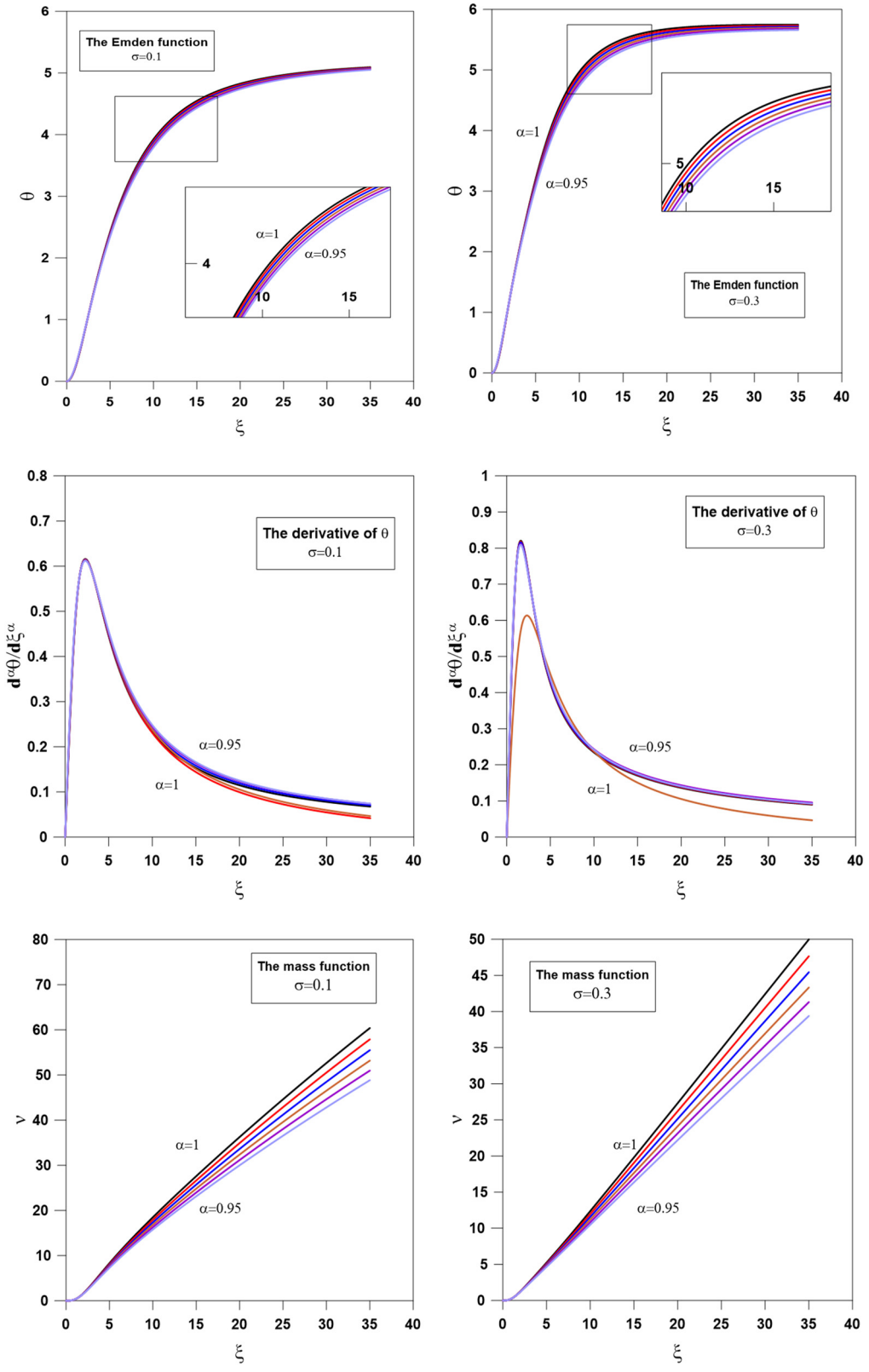

Figure 5: The effect of the fractional parameter on the Emden function (upper panel), the first derivative of the Emden function (middle panel), and the mass function (lower panel). The relativistic parameters are σ = 0.1 and σ = 0.3.

Nevertheless, the fractional derivative has supplemental properties, including a more gradual drop at large radii and smoother behavior at the origin. The graphs demonstrate that the fractional parameter α significantly affects the Emden function. As α drops, the curves become flatter and have a smaller maximum value at a larger radius; this shows how the density of the gas sphere decreases as it gets closer to the center.

The fractional derivative of the Emden function (θ') is shown in the central panel of Figure 5. The radial coordinate ξ is used to represent θ' for different values of the fractional parameter α and relativistic parameter σ. The fact that the curve for $\alpha = 0.95$ is more steep than the curve for $\alpha = 1$ implies that the value of the θ' increase as α decreases. For both σ values ($\sigma = 0.1$ and 0.3), the fractional derivative begins at zero, increases to a peak, and then steadily falls as ξ increases. The larger σ value ($\sigma = 0.3$) has a greater peak value. In both cases, the curve for $\alpha = 1$ is somewhat higher than for $\alpha = 0.95$, especially as ξ increases. The figures show how the fractional derivative of the Emden function fluctuates with the relativistic parameter σ and fractional parameter α. The derivative (θ') is more sensitive to changes in α for higher values of σ, as demonstrated by the greater peak and the significant difference between the curves for various α values in the bottom figure ($\sigma = 0.3$).

The bottom part of Figure 5 shows the mass function (υ) of a fractional isothermal gas sphere (mass within a ξ sphere) for a fractional parameter $\alpha = 0.95$–1 and relativistic parameters $\sigma = 0.1$ and 0.3; for all values of α, the mass function increases with increasing ξ. Smaller values of α result in a slower rate of rise. This is because a slower mass increase results from the fractional derivative's reduction of the effective gravitational force. Additionally, the graph shows that when σ increases, the mass function increases. This is because mass develops quickly due to the relativistic effects' amplification of the gravitational pull. The mass function is zero at $\xi = 0$, increases monotonically with ξ, and increases with rising α and σ.

The mass function at the surface of the gas sphere (*i.e.*, the mass of the gas sphere), $\upsilon(\xi_1)$, as a function of the relativistic parameter (σ), and the fractional parameter (α), is shown in Figure 6. For all values of α, υ (ξ_1) continuously decreases as σ rises. The extent of $\upsilon(\xi_1)$ reduction as σ increases seems to be influenced by the parameter α. The lines representing different values of α illustrate that for increasing values of σ, decreasing α leads to a more pronounced decrease in υ (ξ_1). This suggests that the variable α has the potential to alter the dynamics of the gas sphere or the thermodynamic equations, influencing the variations in physical properties such as compressibility under relativistic conditions. As the value of σ increases, the mass function υ (ξ_1) decreases for all α values. This indicates that relativistic effects decrease the sphere's mass or modify its structure in a way that affects the projected mass function. The gas sphere is more sensitive to increases in σ when α is lower, suggesting a structural or physical change in the gas sphere. α controls how the mass function reacts to changes in σ.

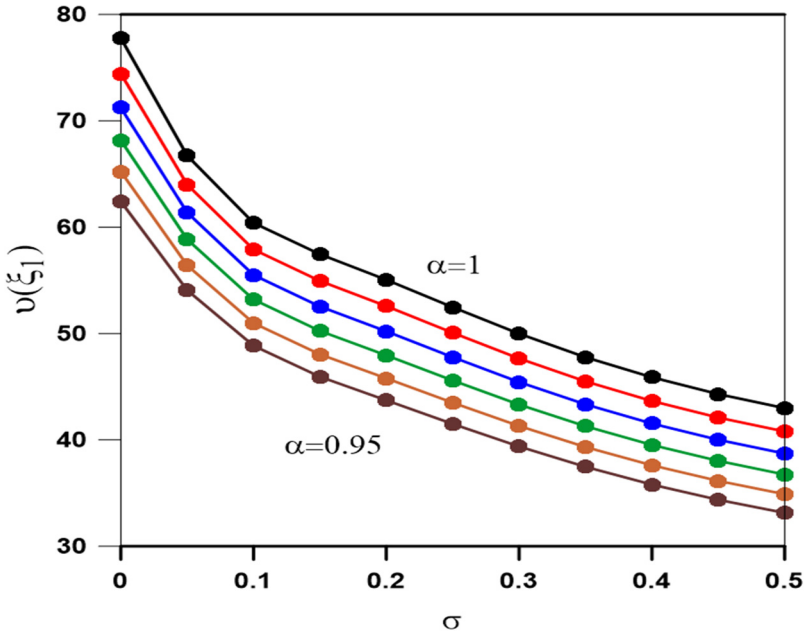

Figure 6: The effect of the relativistic and fractional parameters on the mass function ($\upsilon(\xi_1)$) of the FRISG. The range of $\sigma = 0$–0.5 with $\Delta\sigma = 0.05$ and the range of $\alpha = 0.95$–1 with step $\Delta\alpha = 0.01$.

6 Application for neutron stars

According to some studies, the relativistic isothermal gas sphere is a plausible approximation for middle-aged and ancient neutron stars (>10^5 years). For example, Page [36] indicates that neutron star interiors become almost isothermal during thermal relaxation (~10^4 years), which makes cooling models easier to understand. Tsuruta [37] emphasizes that isothermal models are useful for long-term cooling research since the hydrostatic equilibrium and thermal evolution equations may be separated during this period. Gnedin *et al.* [38] validated isothermal models for older neutron stars by confirming that the whole core retains a relatively uniform temperature until the core and crust thermally equilibrate. According to Tolman's isothermal condition in general relativity, which these models assume, the redshifted temperature stays constant. The isothermal approximation is still a useful tool for researching late-stage neutron star cooling, even though genuine neutron stars may have residual temperature changes because of magnetic fields, superfluidity, and equation of state (EOS) effects.

Under the RISG conditions, a maximum mass exists at which further increases in central density result in instability and collapse [10,39,40]. This observation arises from the interaction of relativistic pressure, density, and gravity. It is vital to highlight that comparing neutron stars with isothermal spheres results in general relativity. Analyzing gravity within the Newtonian framework reveals that the fundamental prerequisite for reaching hydrostatic equilibrium is a connection between the mass density and the pressure, which, for dense matter (degenerate and relativistic), is a power law with adiabatic index γ = 4/3 [39]. But when gravity is considered within the context of general relativity, the TOV equations demand a connection between the mass-energy density and the pressure, which for dense matter is linear. Hence, when exposed to general relativity, the core of neutron stars shows isothermal behavior. Conversely, the core of white dwarf stars, when approached by the limiting mass, is classified as polytropic while being solved using the same EOS as a completely degenerate and ultra-relativistic ideal Fermi gas [10].

The star's mass rises in correlation with the core density until a certain threshold, beyond which relativistic influences play a significant role, leading to the star approaching its maximum mass. This behavior is comparable to that seen in models of white dwarfs, neutron stars, and other compact objects. To investigate the fractional parameter on the central density-mass relation, we follow the approach of Yabushita [40]; the central density may be expressed by $\exp[\theta(\xi)]$ and the mass by $M(\xi)\ \exp[-\theta(\xi)/2]$.

Figure 7 shows the central density-mass relation for the fractional parameters α = 1 and 0.95; the relativistic parameters range from 0.05 to 0.3. While taking into account the relativistic parameter (σ), we may investigate the impact of the fractional parameter (α). We may examine the effects of small deviations from the standard model (α = 1) on the system's characteristics by examining

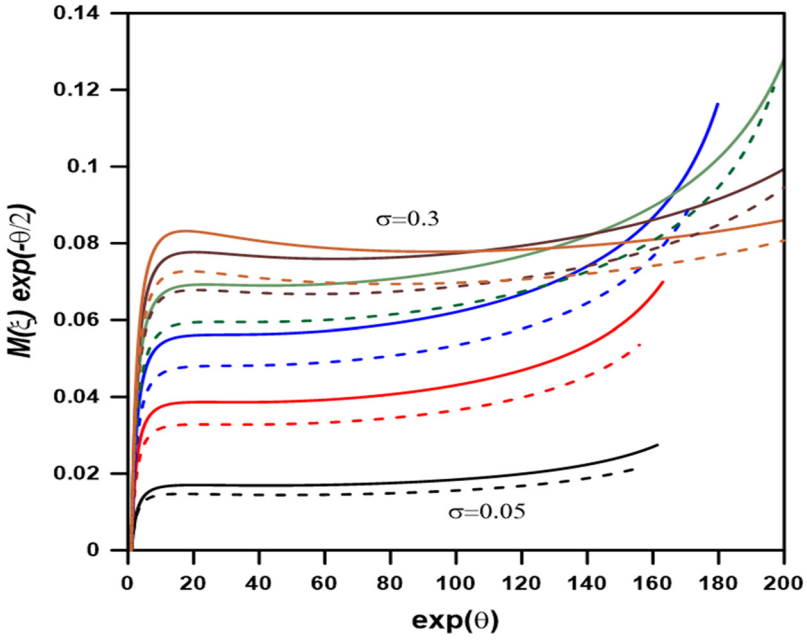

Figure 7: The central density-mass relation for the fractional RISG for α = 1 (solid lines) and α = 0.95 (dashed lines); σ = 0.05–0.3.

how the difference in α from 1 to 0.95 affects the density distribution. For the same σ values throughout the graph, the dashed lines (α = 0.95) usually lie below the solid lines (α = 1). This implies that for a given central density, a decrease in α results in a lower central density. This indicates that a decrease in α results in a less dense central region of the system, which may indicate a decrease in the effective interaction or mass-energy concentration in the sphere's core. Values similar to α and σ in neutron star models might represent the relativistic compactness of the star and the equation of state of the matter in the star, respectively.

Similarly, a lower α (corresponding to a lower core density) might mean that the neutron star has a softer equation of state, making it less resistant to compression under gravity. The impact of the variations in σ on the core density is analogous to the effects of relativistic processes in neutron stars, where greater densities are often attained by increased compactness or gravitational influence up to a certain point (the maximum mass) and then decrease [39,40].

We calculated 18 models with ρ_c, σ, and α as input parameters whose values are appropriate for neutron stars; the results are listed in Table 4. Each row refers to computations for two alternative values of the fractional parameter α (1 and 0.95), with a given relativistic parameter σ = 0.1, demonstrating how differences in α impact the radius and mass for the same central density. The radius continually reduces as α decreases from 1 to 0.95; this suggests that a lower α leads to a more compact arrangement under the same central density circumstances. The mass of the sphere similarly drops with a fall in α. This result shows that the total mass supported by the sphere is smaller when the sphere's structure is impacted by a lower α, potentially suggesting less effective gravitational support or a different distribution of mass inside the sphere.

Table 4: Mass and radius for fractional RISG. The computations are performed for σ = 0.1, α = 0.95 and 1

ρ_c (kg m^{-3})	α = 1		α = 0.95	
	R (m)	M ($M_\odot$)	R (m)	M ($M_\odot$)
2×10^{18}	1.755084×10^4	2.16151	1.710644×10^4	1.72555
3×10^{18}	1.433020×10^4	1.76486	1.396735×10^4	1.40891
4×10^{18}	1.241031×10^4	1.52841	1.209608×10^4	1.22015
5×10^{18}	1.110012×10^4	1.36706	1.081906×10^4	1.09133
6×10^{18}	1.013298×10^4	1.24794	9.876409×10^3	0.99625
7×10^{18}	9.381318×10^3	1.15537	9.143778×10^3	0.92234
8×10^{18}	8.775420×10^3	1.08075	8.541937×10^3	0.86156
9×10^{18}	8.273545×10^3	1.01894	8.064054×10^3	0.81343
1×10^{19}	7.848974×10^3	0.96665	7.650233×10^3	0.77169
2×10^{19}	5.550063×10^3	0.68353	5.409532×10^3	0.54566
3×10^{19}	4.531607×10^3	0.55810	4.416864×10^3	0.44553
4×10^{19}	3.924487×10^3	0.48332	3.825116×10^3	0.38584
5×10^{19}	3.510168×10^3	0.43230	3.421288×10^3	0.34511
6×10^{19}	3.204330×10^3	0.39463	3.123194×10^3	0.31504
7×10^{19}	2.966633×10^3	0.36536	2.891516×10^3	0.29167
8×10^{19}	2.775031×10^3	0.34176	2.704766×10^3	0.27283
9×10^{19}	2.616324×10^3	0.32221	2.550077×10^3	0.25723
1×10^{20}	2.482063×10^3	0.30568	2.419216×10^3	0.24403

Neutron stars are dense, compact stellar remnants with average radii of 1.0×10^4–1.5×10^4 m and masses between 1.4 and 2.5 $M_\odot$. The ranges of radii and masses in the table contain common values for neutron stars, especially at greater core densities. For α = 1, the radius and mass column values align well with those anticipated for neutron stars, particularly at higher densities where the models predict radii and masses within the known range of neutron stars. For α = 0.95, although the radii and masses are often on the lower end, they are realistic for neutron stars, especially for less massive or more compact instances. The models, with their concentration on the fractional isothermal gas sphere utilizing the parameters α and σ, give a theoretical framework that may indeed simulate neutron stars, especially under specific parameter settings (greater central densities and α near to 1). The drop in α leads to more compact and less massive structures, agreeing with some of the changes in neutron stars owing to variances in their equations of state and interior compositions. Thus, these models are instructive but should be understood considering the unique features and the range of circumstances usual for neutron stars.

Now, write the mass of the isothermal gas sphere as

$$M = \frac{4\pi}{3} R^3 \bar{\rho}, \tag{68}$$

where $\bar{\rho}$ is the mean density of the sphere and R is the radius. The mass-radius relation for the isothermal gas sphere is given by

$$M = \frac{4\pi}{3} \rho_c R^3 \frac{\theta'(\xi_1)}{\xi_1}. \tag{69}$$

From the last two equations, we can calculate the central density from

$$\frac{\rho_c}{\bar{\rho}} = \frac{\xi_1}{3\theta'(\xi_1)}. \tag{70}$$

By calculating $\theta'(\xi_1)$ at different values of α, one can obtain the possible values of the central density. For σ = 0.1 and 0.2, we computed models for α = 0.95 and 1. Using the observed radius and mass of neutron stars listed in Table 5,

we determined the mean density in column 4. For different values of σ, α, and ρ_c, we determined the radius of the star from the relation

$$R = \xi_1 \left(\frac{4\pi G \rho_c}{\alpha \sigma c^2} \right)^{-3/2}. \quad (71)$$

Given its unlimited radius, the relativistic isothermal gas sphere does provide a conceptual problem. However, when using the FRISG model to model neutron stars, several physical factors enable us to operate with limited, reasonable values of the dimensionless radius ξ_1 by adding pragmatic restrictions in neutron stars.

Figure 8 locates the observed mass and radius of neutron stars on the mass-radius relationship of the fractional RISG along with the mass and radius of the three neutron stars: PSR J1614-2230 with mass $M = 1.97 \pm 0.04\,M_\odot$ and radius $R = 1.3 \times 10^4 \pm 2{,}000$ m [41,42]. J0437-4715 with mass $M = 1.44 \pm 0.07\,M_\odot$ and radius $R = 1.36 \times 10^4 \pm 900$ m [43,44]. SAXJ1808.4–3658 with $M = 0.9 \pm 0.3\,M_\odot$ and radius $R = 7.951 \times 10^3 \pm 1{,}000$ m [44,45]. The physical parameters of the theoretical models are listed in Table 5. The solid lines represent the predicted mass-radius relationship for neutron stars with $\alpha = 1$, and the dashed lines are with $\alpha = 0.95$. Table 5 shows that the FRISG model suggested for the three stars agrees with the observed values, considering the errors due to observations.

The value of α influences the predicted mass for a given radius, influencing the EOS that the models utilize. As observed, small variations in α lead to different expected mass-radius relationships, affecting the EOS. Higher σ values, which affect the neutron star's mass for a given radius, often suggest a denser core or a different composition. Denser neutron stars have a substantially larger mass at any given radius than less dense ones, as seen by the models with larger σ values (red lines), which exhibit a steeper mass-radius relationship. The estimated mass for a given radius decreases dramatically when the fractional parameter is reduced from 1 to 0.95, indicating the sensitivity of the expected neutron star properties to the EOS parameters. Changes in parameters may provide a more accurate description of neutron star design since the dotted lines (for $\alpha = 0.95$) seem to fit the observed data points better than the solid lines (for $\alpha = 1$). This may be considered for understanding the effects of model parameters (α, σ, and EOS) on expected neutron star physical characteristics and how they match with observational data.

The observed parameters of the star PSR J1614–2230 are $M = 2.08\,M_\odot$, $R = 1.396 \times 10^4$ m, and the optimal parameters are $\sigma = 0.2$, $\alpha = 0.95$, $\rho_c = 3.0 \times 10^{18}$ kg/m^3, $P_c = 5.4 \times 10^{34}$ N/m^2. A mass of ~2 $M_\odot$ requires strong relativistic corrections, hence a moderate relativistic parameter $\sigma = 0.2$. The choice of $\alpha = 0.95$ reflects the need to slightly soften the internal pressure gradient, allowing for a denser but still stable configuration. The central density $\rho_c = 3.0 \times 10^{18}$ kg/m^3 is consistent with expectations for massive neutron stars and helps generate the required gravitational pressure. The star J0437–4715 have an observed $M = 1.40\,M_\odot$, $R = 1.396 \times 10^4$ m, and the optimal parameters are $\sigma = 0.1$, $\alpha = 0.95$, $\rho_c = 3.0 \times 10^{18}$ kg/m^3, $P_c = 2.7 \times 10^{34}$ N/m^2. A slightly lower mass (~1.4 $M_\odot$) allows for a smaller relativistic correction, so a weaker relativistic parameter $\sigma = 0.1$ is sufficient. Again, $\alpha = 0.95$ is used to adjust the mass–radius curve downward, ensuring consistency with observations despite a lower central pressure than PSR J1614–2230. Same central density as PSR J1614–2230 implies similar internal composition, but the lower mass and pressure suggest that it is a less compact configuration. For the star SAX J1808.4–3658, the observed values of the mass and radius are $M = 0.77\,M_\odot$, $R = 7.65 \times 10^3$ m. The optimal parameters are $\sigma = 0.1$, $\alpha = 0.95$, $\rho_c = 1.0 \times 10^{19}$ kg/m^3, and $P_c = 9.0 \times 10^{34}$ N/m^2. Although the mass is relatively low, the radius is extremely small, indicating a very compact object. To produce such a compact structure under relatively low mass, a very high central density $\rho_c = 10^{19}$ kg/m^3 is required. The low $\alpha = 0.95$ again serves to soften the system structurally and produce a realistic mass-radius curve for such a dense star. Despite low mass, the high pressure indicates an unusual internal EOS, possibly due to phase transitions or strong-field effects (*e.g.*, quark deconfinement). Summarizing the results, fractional model systems with nonlocal internal structure, *i.e.*, deviations from ideal hydrostatic profiles. It softens the equation of state, leading to more compact but stable configurations. Introduces stronger relativistic corrections (*i.e.*, compactness), needed for more massive stars. Compensates (ρ_c, central density)

Table 5: Predicted FRISG physical parameters of three neutron stars

Object	M ($M_\odot$)	R (m)	$\bar{\rho}$ (kg m^{-3})	σ	α	ρ_c (kg m^{-3})	P_c (N m^{-2})
PSR J1614-2230	2.08	1.396×10^4	4.256×10^{17}	0.2	0.95	3.0×10^{18}	5.4×10^{34}
J0437-4715	1.40	1.396×10^4	2.717×10^{17}	0.1	0.95	3.0×10^{18}	2.7×10^{34}
SAXJ1808.4–3658	0.77	7.65×10^3	8.498×10^{17}	0.1	0.95	1.0×10^{19}	9.0×10^{34}

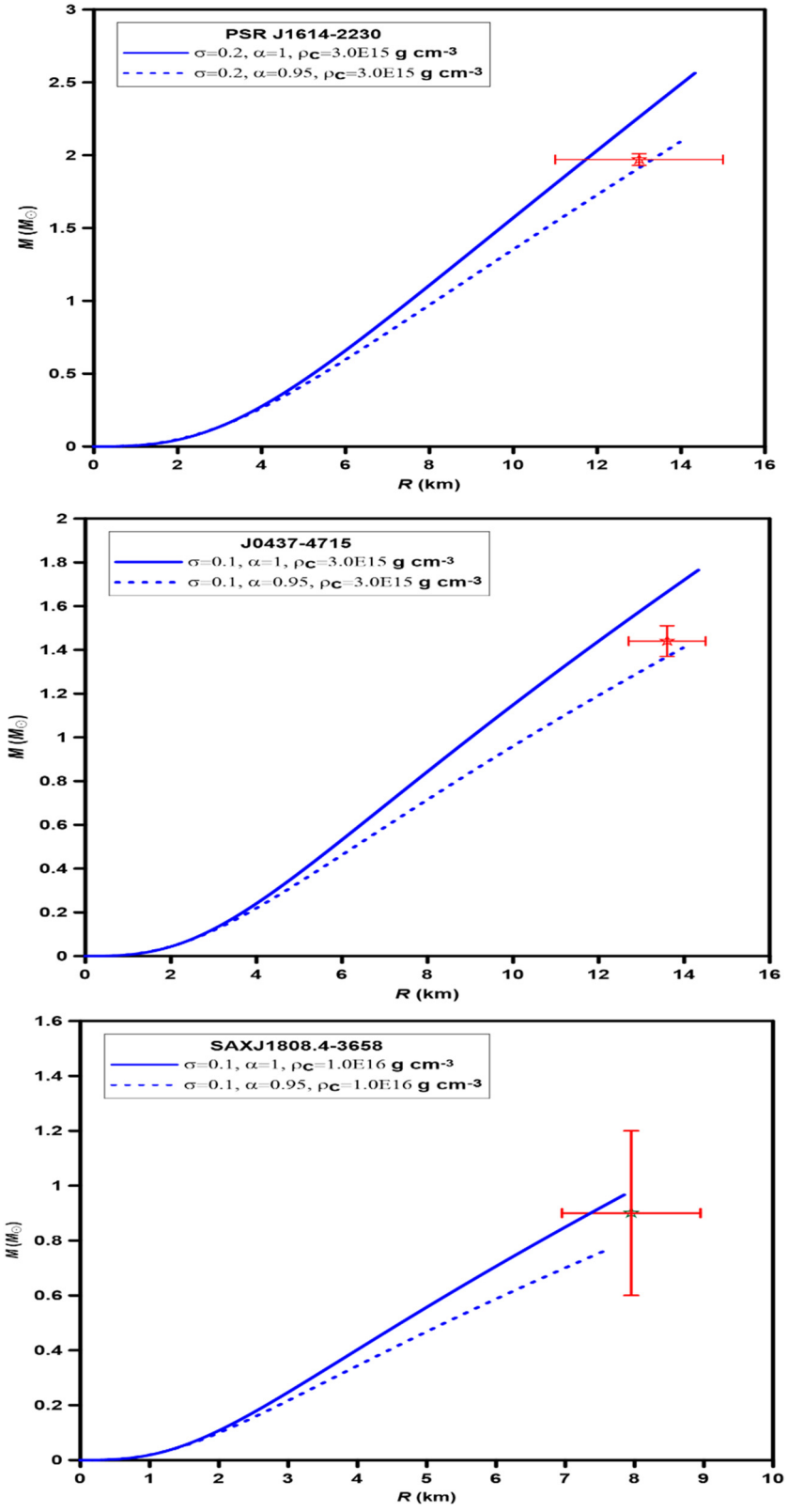

Figure 8: The mass-radius relation for the three observed neutron stars PSR J1614-2230, J0437-4715, and SAXJ1808.4–3658. The predicted physical parameters for PSR J1614-2230 are σ = 0.2, α = 0.95, and ρ_c = 3.0 × 10^{18} kg m^{-3}; for the star J0437-4715, the predicted physical parameters are σ = 0.1, α = 0.95, and ρ_c = 3.0 × 10^{18} kg m^{-3}; for SAXJ1808.4–3658, the predicted values are σ = 0.1, α = 0.95, and ρ_c = 1.0 × 10^{19} kg m^{-3}.

for smaller radii or lower masses by increasing pressure to prevent collapse.

With instability and collapse occurring beyond a critical mass or density, Chavanis [10,11] showed that the stability and equilibrium of isothermal spheres, including slowly rotating and polytropic cases, are controlled by turning points in the energy-temperature or central density-mass diagrams. This behavior is reflected in the maximum mass and the onset of instability of the FRISG. The present work's findings, which include the existence of a maximum mass and the qualitative features of the mass-radius and central density-mass relations, directly parallel these relativistic isothermal predictions. Chavanis [12] also demonstrated that relativistic stars with a linear equation of state, such as neutron star cores, behave similar to isothermal spheres in general relativity, exhibiting a spiral mass-radius relation and a critical mass-energy threshold. Adding α as an extra degree of freedom, the fractional approach used in the present study generalizes these classical and relativistic results. This allows for continuous tuning of neutron stars' stability boundary and structural properties, capturing a wider range of physical behaviors and possibly reflecting nonlocal or microphysical effects that are not considered in standard models. This illustrates how the addition of fractional calculus enhances the theoretical landscape for modeling compact objects by offering a flexible phenomenological framework that can interpolate between various regimes of stability and compactness, by both classical and contemporary astrophysical theory, while also preserving the key elements of maximum mass and gravitational instability found in Chavanis' work.

Also, the present study shows that sharper density profiles and more condensed, centrally concentrated mass distributions result from both reducing the fractional parameter (α) and raising the relativistic parameter (σ). Notably, the occurrence of a maximum mass, beyond which the structure collapses and becomes unstable, is consistent with previous discoveries utilizing fractional polytropic models and reflects the well-known behavior in classical TOV solutions for neutron stars [30]. Neutron star models that have softer equations of state and lower values are less compact. Particularly because of gravitational wave and NICER evidence, this is consistent with recent observational constraints and theoretical models that imply a range of stiffness in neutron star equations of state [46,47]. As a result, the fractional method offers a versatile framework for interpolating across various physical regimes and might contribute to the explanation of the variety of observable neutron star characteristics. The function of exotic matter and phase transitions (such as hadron-quark deconfinement) in neutron star interiors has been the subject of more recent studies. The fractional parameter α might be viewed as a phenomenological proxy for nonlocal interactions or changes in the effective equation of state, perhaps capturing some features of these transitions, even if the current study does not specifically address such microphysical effects. Neutron stars with quantum chromodynamics phase transitions, for example, exhibit sudden changes in neutrino and gravitational wave signals and changes in the mass-radius relation effects [47], which might theoretically be reproduced by adjusting α in the fractional model.

7 Conclusion

This work expands the TOV equation of the relativistic isothermal gas sphere to include fractional derivatives (FRISG), leading to a more comprehensive FTOVI. An accelerated series expansion is used to solve the FTOVI analytically. We calculated models for different values of the relativistic (σ) and fractional (α) parameters. We found that models having α value of 1 are limited to the relativistic integer models derived from the TOV equation. We can summarize the results in the following points:

- The classical isothermal model assumes a constant temperature throughout the gas sphere. This simplification is typically valid for systems where heat transfer processes quickly equalize temperature differences. The resulting equation of hydrostatic equilibrium leads to the classical isothermal TOV equation, where thermal gradients are not dominant drivers of the structure. However, real stars may not be perfectly isothermal. Small deviations from temperature uniformity are physically present but can be negligible if other structural effects dominate. As revealed from the results, changing the fractional order α has a significant impact on solutions: altering density profiles, pressure distribution, and mass-radius relations. These structural changes outweigh the impact of mild temperature gradients. Mathematically, a small spatial variation in temperature would contribute a perturbative correction to the pressure, but fractional derivatives globally reshape the differential structure of the model. Hence, while nonuniform temperature introduces second-order corrections (they perturb an existing model without fundamentally altering its structure) in thermodynamic quantities, conformable modeling introduces first-order changes (instead of just altering their inputs, they substitute the fundamental operators in the governing equations) in the system's physical behavior, particularly pressure

support, gravitational stability, radius and mass distribution, and central condensation.

- In the context of fractional relativistic isothermal spheres, the behavior of the Emden function, the mass function, and the first fractional derivative of the Emden function for various α values offer valuable insights into how changes in fundamental structural parameters can influence the physical properties of dense astrophysical objects, such as neutron stars. Lower α values correspond to lower central densities, suggesting a softer structural composition. These findings align with observations of neutron stars that exhibit a softer equation of state, which has implications for understanding their stability and evolution. Such insights can aid in refining neutron star formation and behavior models, ultimately enhancing our comprehension of these complex cosmic entities.
- Increasing the relativistic parameter σ (or decreasing the fractional parameter α) results in more condensed and sharply declining profiles in the FRISG. These changes highlight the enhanced gravitational and compact effects associated with these parameters. The variations in the mass function illustrate how these factors influence the mass distribution within the sphere, with larger values leading to a greater amount of mass at any given radius.
- Utilizing fractional calculus to study the FRIGS provides deeper insights into their thermodynamic balance, stability, and dynamic evolution under extreme conditions. Future research should prioritize developing theoretical models, validating predictions against observational data, and exploring innovative applications across various astrophysical scenarios. Notably, a maximum mass exists within the framework of the relativistic isothermal gas sphere; beyond a certain central density, the system becomes unstable and may collapse. This phenomenon arises from the complex interplay of relativistic pressure, density, and gravitational forces. As the core density increases, the mass of the FRISG grows until it reaches a critical threshold, after which relativistic effects become significant, resulting in the system achieving its maximum mass. This behavior mirrors what is observed in neutron star models and other compact objects, enhancing our understanding of their formation and stability.
- Testing the mass-radius relationship of the FRISG against the observed masses and radii of three neutron stars shows good agreement when the fractional parameter is less than 1. These findings can be further explored to assess how theoretical parameters, such as α, σ, and central density, affect the physical properties of neutron stars and how well these predictions align with observational data. This understanding could enhance models of neutron star behavior, improve our grasp of their internal structures, and potentially inform searches for new astrophysical phenomena related to these enigmatic objects.

Acknowledgments: The authors extend their appreciation to Northern Border University, Saudi Arabia, for supporting this work through project number (NBU-CRP-2025-1266).

Funding information: Researchers Supporting Program Number (NBU-CRP-2025-1266), Northern Border University, Arar, Saudi Arabia.

Author contributions: Mohamed Nouh and Emad Abdel-Salam: writing – review and editing, writing – original draft, validation, software, methodology, and conceptualization. Abaker Hassaballa: writing – original draft. M. S. Jazmati: writing – original draft. All authors have accepted responsibility for the entire content of this manuscript and approved its submission.

Conflict of interest: The authors state no conflict of interest.

Data availability statement: All data generated or analyzed during this study are included in this published article.

References

[1] Chandrasekhar S. An introduction to the study of stellar structure. Chicago: University of Chicago Press; 1939.
[2] Tolman RC. Relativity, thermodynamics, and cosmology. Oxford: Clarendon Press; 1934.
[3] Oppenheimer JR, Volkoff GM. On massive neutron cores. Phys Rev. 1939;55:374.
[4] Nouh MI, Foda MM, Aboueisha MS. Compact stars with non-uniform relativistic polytrope. Sci Rep. 2024;14:16237. doi: 10.1038/s41598-024-65973-7.
[5] Glendenning NK. General relativity and compact stars. In Centennial of general relativity: A celebration. Singapore: World Scientific Pub Co Inc.; 2017. p. 1–72. doi: 10.1142/9789814699662_0001.
[6] Chau WY, Lake K, Stone J. Static structure of general relativistic, partially degenerate, self-gravitating, lepton configurations. I Numerical scheme. Astrophys J. 1984;281:560. doi: 10.1086/162129.
[7] Edwards TW, Merilan MP. Partially degenerate semirelativistic isothermal spheres of arbitrary temperature. Astrophys J. 1981;244:600. doi: 10.1086/158740.
[8] Edwards TW, Merilan MP. Numerical function values for slowly rotating partially degenerate semirelativistic isothermal spheroids

of arbitrary temperature. Astrophys J Suppl Ser. 1981;47:291. doi: 10.1086/190761.
[9] Sharma JP. Some relativistic features of nonrotating isothermal spheres - Motivation and numerical relativity. Astrophys Space Sci. 1990;163:109–25. doi: 10.1007/BF00639981.
[10] Chavanis PH. Gravitational instability of slowly rotating isothermal spheres. Astron Astrophys. 2002;381:709. doi: 10.1051/0004-6361:20011424.
[11] Chavanis PH. Gravitational instability of isothermal and polytropic spheres. Astron Astrophys. 2003;401:15. doi: 10.1051/0004-6361:20021779.
[12] Chavanis PH. Relativistic stars with a linear equation of state: analogy with classical isothermal spheres and black holes. Astron Astrophys. 2008;483:673. doi: 10.1051/0004-6361:20078287.
[13] Stanislavsky AA. Astrophysical applications of fractional calculus. In: Haubold H, Mathai A, editors. Proceedings of the Third UN/ESA/NASA Workshop on the International Heliophysical Year 2007 and Basic Space Science. Astrophysics and Space Science Proceedings. Berlin, Heidelberg: Springer; 2010.
[14] Jamil M, Momeni D, Rashid MA. Fractional action cosmology with power law weight function. J Phys: Conf Ser. 2012;354:012008.
[15] El-Nabulsi RA. Gravitons in fractional action cosmology. Int J Theor Phys. 2012;51:3978.
[16] Shchigolev VK. Cosmological models with fractional derivatives and fractional action functional. Commun Theor Phys. 2011;56:389.
[17] Shchigolev VK. Testing fractional action cosmology. Eur Phys J Plus. 2016;131:256.
[18] El-Nabulsi RA. Fractional derivatives generalization of Einstein's field equations. Indian J Phys. 2013;87:195.
[19] El-Nabulsi RA. A family of Emden–Fowler differential equations from a generalized derivative operator. J Anal. 2017;25:301.
[20] El-Nabulsi RA. Implications of the Ornstein-Uhlenbeck-like fractional differential equation in cosmology. Rev Mexicana de Fısica. 2016;62:240.
[21] Mirza B. Approximate analytical solutions of the Lane-Emden equation for a self-gravitating isothermal gas sphere. Mon Not R Astron Soc. 2009;395:2288.
[22] Nouh MI. Computational method for a fractional model of the helium burning network. N Astron. 2019;66:40.
[23] Yousif E, Adam A, Hassaballa A, Nouh MI. Conformable isothermal gas spheres. N Astron. 2021;84:101511.
[24] El-Nabulsi RA. The fractional white dwarf hydrodynamical nonlinear differential equation and emergence of quark stars. Appl Math Comput. 2011;218:2837.
[25] Bayin SS, Krisch JP. Fractional incompressible stars. Astrophys Space Sci. 2015;359:58.
[26] Abdel-Salam EAB, Nouh MI. Approximate solution to the fractional second-type lane-emden equation. Astrophysics. 2016;59:398–410.
[27] Nouh MI, Abdel-Salam EA-B. Analytical solution to the fractional polytropic gas spheres. Eur Phys J Plus. 2018;133:149.
[28] Abdel-Salam EA-B, Nouh MI. Conformable polytropic gas spheres. N Astron. 2020;76:101322.
[29] Abdel-Salam EA-B, Nouh MI, Elkholy EA. Analytical solution to the conformable fractional Lane-Emden type equations arising in astrophysics. Sci Afr. 2020;8:e00386. doi: 10.1016/j.sciaf.2020.e00386.
[30] Aboueisha MS, Nouh MI, Abdel-Salam EA-B, Kamel TM, Beheary MM, Gadallah KAK. Analysis of the fractional relativistic polytropic gas sphere. Sci Rep. 2023;13:14304. doi: 10.1038/s41598-023-41392-y.
[31] Khalil R, Al-Horani M, Yousef A, Sababheh MJ. Comput Appl Math. 2014;264:65.
[32] Hunter C. Series solutions for polytropes and the isothermal sphere. Mon Not R Astron Soc. 2001;328(3):839–47.
[33] Nouh MI. Accelerated power series solution of the polytropic and isothermal gas spheres. N Astron. 2004;9:467.
[34] Saad A-NS, Nouh MI, Shaker AA, Kamel TM. Stability analysis of relativistic polytropes. Rev Mexicana de Astronomia y Astrofisica. 2021;57:407.
[35] Demodovich B, Maron I. Computational mathematics. Moscow: Mir Publishers; 1973.
[36] Page D. Fast cooling of neutron stars: Superfluidity versus heating and accreted envelope. Astrophys J. 1997;479(1):L43–6. IOP. doi: 10.1086/310571.
[37] Tsuruta S. Thermal evolution of neutron stars-current status. In Quarks and compact stars 2017 (QCS2017). 2018;20:Art. no. 011001. doi: 10.7566/JPSCP.20.011001.
[38] Gnedin OY, Yakovlev DG, Potekhin AY. Thermal relaxation in young neutron stars. Mon Not R Astron Soc. June 2001;324(3):725–36. doi: 10.1046/j.1365-8711.2001.04359.x.
[39] Misner CW, Zapolsky HS. High-density behavior and dynamical stability of neutron star models. Phys Rev Lett. 1964;12:635.
[40] Yabushita S. On the analogy between neutron star models and isothermal gas spheres and their general relativistic instability. Mon Not R Astron Soc. 1974;167:95. doi: 10.1093/mnras/167.1.95.
[41] Demorest P, Pennucci T, Ransom S, Roberts M, Hessels J. A two-solar-mass neutron star measured using Shapiro delay. Nature. 2010;467:1081.
[42] Crawford F, Roberts MS, Hessels JW, Ransom SM, Livingstone M, Tam CR, et al. A survey of 56 midlatitude EGRET error boxes for radio pulsars. Astrophys J. 2006;652(2):1499–1507. arXiv: astro-ph/0608225).
[43] Reardon DJ, Hobbs G, Coles W, Levin Y, Keith MJ, Bailes M, et al. MNRAS. 2016;455:1751. arXiv:1510.04434 [astro-ph.HE].
[44] González-Caniulef D, Guillot S, Reisenegger A. Neutron star radius measurement from the ultraviolet and soft X-ray thermal emission of PSR J0437− 4715. Mon Not R Astron Soc. 2019;490:5848. arXiv:1904.12114 [astro-ph.HE].
[45] Wijnands R, van der Klis M. A millisecond pulsar in an X-ray binary system. Nature. 1998;394(6691):344–6.
[46] Celi MO, Mariani M, Kumar R, Bashkanov M, Orsaria MG, Pastore A, et al. Exploring the role of d* hexaquarks on quark deconfinement and hybrid stars. arXiv:250400981. 2025. doi: 10.48550/arXiv.2504.00981.
[47] Khosravi Largani N, Fischer T, Shibagaki S, Cerda-Duran P, Torres-Forne A. Neutron stars in accreting systems–Signatures of the QCD phase transition. Astron Astrophys. 2024;687:A245. doi: 10.1051/0004-6361/202348742.